Review

José Manuel Luque-González*, Alejandro Sánchez-Postigo, Abdelfettah Hadij-ElHouati, Alejandro Ortega-Moñux, J. Gonzalo Wangüemert-Pérez, Jens H. Schmid, Pavel Cheben, Íñigo Molina-Fernández and Robert Halir

A review of silicon subwavelength gratings: building break-through devices with anisotropic metamaterials

https://doi.org/10.1515/nanoph-2021-0110
Received March 15, 2021; accepted July 19, 2021;
published online August 12, 2021

Abstract: Silicon photonics is playing a key role in areas as diverse as high-speed optical communications, neural networks, supercomputing, quantum photonics, and sensing, which demand the development of highly efficient and compact light-processing devices. The lithographic segmentation of silicon waveguides at the subwavelength scale enables the synthesis of artificial materials that significantly expand the design space in silicon photonics. The optical properties of these metamaterials can be controlled by a judicious design of the subwavelength grating geometry, enhancing the performance of nanostructured devices without jeopardizing ease of fabrication and dense integration. Recently, the anisotropic nature of subwavelength gratings has begun to be exploited, yielding unprecedented capabilities and performance such as ultrabroadband behavior, engineered modal confinement, and sophisticated polarization management. Here we provide a comprehensive review of the field of subwavelength metamaterials and their applications in silicon photonics. We first provide an in-depth analysis of how the subwavelength geometry synthesizes the metamaterial and give insight into how properties like refractive index or anisotropy can be tailored. The latest applications are then reviewed in detail, with a clear focus on how subwavelength structures improve device performance. Finally, we illustrate the design of two ground-breaking devices in more detail and discuss the prospects of subwavelength gratings as a tool for the advancement of silicon photonics.

Keywords: all-dielectric metamaterials; anisotropic homogenization; high-performance devices; silicon photonics; subwavelength gratings structures.

1 Introduction

Optical metamaterials are synthetic structures with physical properties that are not readily accessible in nature. The most exotic metamaterial properties are attained via resonant structures, which induce substantial changes in the properties of light over distances comparable to the free-space wavelength, thereby enabling the realization of ultra-thin metasurface components [1–6]. Nonresonsant dielectric structures at the subwavelength scale, on the other hand, behave as effective homogeneous media with an anisotropic refractive index tensor [7]. Subwavelength grating metamaterials, since their first demonstration in integrated silicon waveguides at NRC Canada [8–16], are playing a crucial role in the field of silicon photonics [17, 18]. Silicon photonics leverages the advanced nanofabrication infrastructure established by the complementary metal–oxide–semiconductor (CMOS) microelectronics industry to drive key advances in areas as diverse as datacom and telecom [19], metrology [20], biochemical sensing [21, 22], quantum signal processing [23], and light detection and ranging (LiDAR) [24]. While the large refractive index contrast between silicon ($n_{Si} \approx 3.5$) and its native oxide ($n_{SiO_2} \approx 1.45$) enables dense integration, the scarcity of CMOS-compatible materials with intermediate refractive indices restricts the design space. This limitation can be overcome by structuring silicon waveguides at the

***Corresponding author: José Manuel Luque-González**, Telecommunication Research Institute (TELMA), Universidad de Málaga, CEI Andalucía TECH, Louis Pasteur 35, 29010 Málaga, Spain, E-mail: jmlg@ic.uma.es. https://orcid.org/0000-0002-6838-8641
Alejandro Sánchez-Postigo, Abdelfettah Hadij-ElHouati, Alejandro Ortega-Moñux, J. Gonzalo Wangüemert-Pérez, Íñigo Molina-Fernández and Robert Halir, Telecommunication Research Institute (TELMA), Universidad de Málaga, CEI Andalucía TECH, Louis Pasteur 35, 29010 Málaga, Spain
Jens H. Schmid and Pavel Cheben, National Research Council Canada, Ottawa, Ontario, Canada

subwavelength scale. Using a single, full etch step, a wide range of equivalent anisotropic materials can be synthesized [18]. This concept is schematically illustrated in Figure 1, which compares the propagation through a silicon waveguide structured at subwavelength scale, and the propagation through the equivalent anisotropic waveguide. Indeed, the flexibility enabled by silicon subwavelength grating (SWG) structures has led to breakthrough advances in many areas of silicon photonics, including broadband, ultra efficient fiber-to-chip couplers [25–27], high-performance integrated filters [28, 29], power and polarization splitters covering several optical communication bands [30, 31], on-chip graded-index (GRIN) lenses [32], evanescent field control [33], or even the exploration of non-Hermitian systems [34]. At telecom wavelengths, the feature sizes required for subwavelength operation are ~100 nm, which is why most subwavelength-based devices reported so far have been fabricated with e-beam lithography. However, significant advances in deep-ultraviolet immersion lithography now enable volume fabrication of structures with sub-100-nm feature sizes [35, 36], and several subwavelength-based devices are already mass fabricated [37–39].

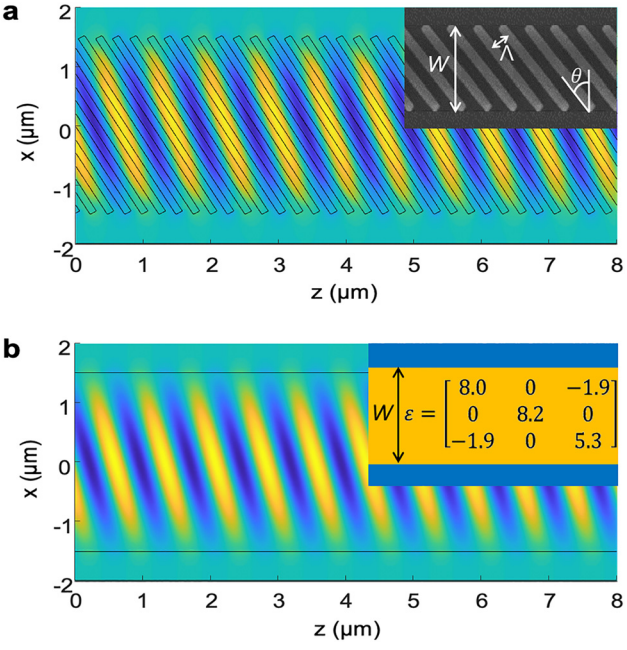

Figure 1: Simulated propagation of the electric field through (a) a tilted subwavelength waveguide and (b) the equivalent homogeneous anisotropic waveguide. Linear polarization in the x–z plane and a free-space wavelength of 1.55 μm are considered. In both (a) and (b), the geometry of the waveguide is outlined in black. The waveguide layer is 220 nm thick and 3 μm wide. In (a), $\Lambda = 250$ nm, DC = 0.5 and $\theta = 30°$. In (b) the permittivity tensor of the waveguide core metamaterial is shown.

As the pace of progress in the field of silicon subwavelength structures continues to accelerate, in this review we aim to provide a comprehensive and insightful overview of the latest developments. Following the approach of our previous reviews on the topic [18, 40, 41], we start with an in-depth discussion of the most up-to-date knowledge of the foundations of subwavelength structures: in Section 2 we study to how and to what extent these structures can be modeled as homogeneous anisotropic metamaterials. The optical properties of these metamaterials are instrumental in understanding how subwavelength structures are exploited to enhance each family of devices we revise in Section 3: waveguides, broadband couplers, beam expanders, polarization controllers, filters, wavelength- and mode-division multiplexing devices, fiber-chip couplers, optical antennas, and evanescent field sensors. In Section 4 we simulate a small selection of cutting-edge subwavelength-based devices, emphasizing how the optical properties of subwavelength structures are exploited and illustrating how the anisotropic modeling and the appropriate electromagnetic tools help efficiently design those devices. Finally, in Section 5 conclusions are drawn and a short outlook is provided.

2 Understanding silicon subwavelength metamaterials

The core idea underlying subwavelength gratings is that they enable us to synthesize integrated optical materials with tailorable properties. To exploit the full potential of these structures, it is crucial to understand under which conditions periodic structures act as equivalent homogeneous materials and what exactly the properties of these materials are.

To illustrate the main goal of this section, let us examine the segmented silicon waveguide shown in Figure 2(a). This structure is periodic in the longitudinal direction (z) and is therefore described rigorously by modal analysis using the Floquet–Bloch theory. Light propagates through this dielectric waveguide with no loss when the period (Λ) is below the Bragg threshold, i.e., $\Lambda < \lambda_0/(2n_{\text{eff}})$, where λ_0 is the operating wavelength (in vacuum) and n_{eff} is the effective index of the fundamental Floquet–Bloch mode supported by the structure. Under this condition, the periodic waveguide operates in the subwavelength regime and effectively behaves as a solid-core waveguide with the equivalent core material that is described by the permittivity tensor $\boldsymbol{\varepsilon} = \text{diag}[n_{xx}^2, n_{yy}^2, n_{zz}^2]$. The technique that yields the values of the tensor components is known as *homogenization* and is

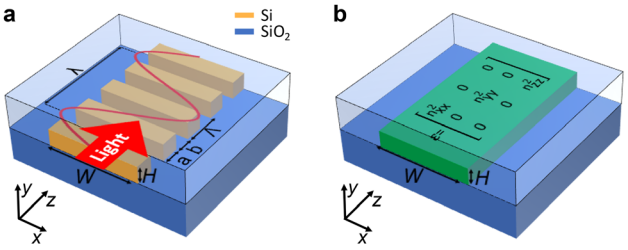

Figure 2: (a) Schematic of a longitudinal SWG waveguide. The period of the structure, Λ, is much shorter than the guided wavelength, λ, of the light propagating along the z-axis. (b) Schematic of the homogeneous waveguide model of the structure shown in (a). The SWG waveguide core is modeled as a homogeneous anisotropic medium with a permittivity tensor $\boldsymbol{\varepsilon}$.

used to model the actual subwavelength waveguide as a homogeneous anisotropic metamaterial waveguide. The simulation of the equivalent, homogenized structure is substantially less time-consuming than rigorous Floquet–Bloch analysis of the SWG waveguide and provides useful physical insight on how SWG-based high-performance integrated devices work. In this section, we will study the behavior of subwavelength waveguides and how to accurately homogenize them.

The accuracy of the homogenization process decreases as the ratio Λ/λ approaches the Bragg regime since the resonances within the photonic bandgap cannot be described by a homogeneous metamaterial. In the following we will present two modeling methods and compare the results they provide with the rigorous Floquet–Bloch solution of the subwavelength waveguide:

- An analytical laminar model of the subwavelength material, which is adequate for most applications as long as the vicinity of the Bragg threshold is avoided (Section 2.1).
- A more sophisticated slab model that takes into account the thickness of the silicon waveguide layer and provides accurate results even when the waveguide operates near the Bragg regime (Section 2.2).

These models will be used to approximate subwavelength waveguides with longitudinal (z-periodic) and transverse (x-periodic) segmentations, while more complex (tilted) periodic patterns will be analyzed in Section 2.3.

Throughout this section we will assume typical material parameters for silicon photonics: $n_{Si} = 3.476$, $n_{SiO_2} = 1.444$, a duty cycle directional coupler (DC) = a/Λ = 0.5, and a silicon thickness H = 220 nm, operating at a wavelength $\lambda_0 = 1.55$ µm. The width of the waveguide is W = 3 µm. For illustration purposes we consider pitches of Λ = 50 nm, which is in the long-wave limit ($\Lambda \ll \lambda$), and Λ = 220 nm, which can be readily fabricated with modern lithography techniques and is still below the Bragg threshold, $\Lambda_{Bragg}^{wg} = 300$ nm for our exemplary waveguide. For the sake of simplicity, we assume that the cladding and substrate are the same materials. We furthermore refer to light polarized along the y-axis as transverse magnetic (TM) polarized, and light polarized along the x- or z-axis as transverse electric (TE) polarized.

2.1 Laminar material model

The laminar model considers the subwavelength structure as a cut-out of an infinite laminar arrangement of two materials with period Λ, as illustrated in Figure 3(a). The material laminae have refractive indices $n_1 = n_{Si}$ and $n_2 = n_{SiO_2}$, and lengths a = DC·Λ and b = (1 − DC)·Λ, respectively. To obtain the equivalent permittivity tensor of the laminar material, we take into account the propagation of TE and TM plane waves in the x–z plane. Specifically, we study the wave vector, $k = k_x\hat{x} + k_z\hat{z}$, for different propagating angles $\phi = \tan^{-1}(k_x/k_z)$ [see Figure 3(a)]. The wave vector components (k_x and k_z) are calculated using the dispersion relations [42]:

$$\cos(k_z\Lambda) = \cos(k_{1z}a)\cos(k_{2z}b) - \Delta_{TE}\sin(k_{1z}a)\sin(k_{2z}b), \quad (1)$$

$$\cos(k_z\Lambda) = \cos(k_{1z}a)\cos(k_{2z}b) - \Delta_{TM}\sin(k_{1z}a)\sin(k_{2z}b), \quad (2)$$

for TE and TM polarizations, respectively, where $k_{iz} = \sqrt{(k_0 n_i)^2 - k_x^2}$, and Δ is a polarization-dependent factor:

$$\Delta_{TE} = \frac{1}{2}\left(\frac{n_2^2}{n_1^2}\frac{k_{1z}}{k_{2z}} + \frac{n_1^2}{n_2^2}\frac{k_{2z}}{k_{1z}}\right), \quad \Delta_{TM} = \frac{1}{2}\left(\frac{k_{1z}}{k_{2z}} + \frac{k_{2z}}{k_{1z}}\right). \quad (3)$$

These equations fully characterize the propagation of a plane wave along the laminar periodic structure for any period-to-wavelength ratio. However, in this review we focus on the subwavelength regime, which for the particular laminar structure we are considering implies using a pitch $\Lambda < \Lambda_{Bragg}^{lam} = 240$ nm. Since the laminar material is infinite, the effective indices of the Floquet–Bloch modes are larger than in the subwavelength-structured waveguide, and hence the Bragg threshold of the laminar material is smaller than that of the subwavelength waveguide ($\Lambda_{Bragg}^{lam} < \Lambda_{Bragg}^{wg}$). In any case, in the long-wave limit, $\Lambda \ll \lambda$, we have $k_z\Lambda \ll 1$ (and hence $k_{1z}a \ll 1$ and $k_{2z}b \ll 1$), so that Eqs. (1) and (2) simplify to

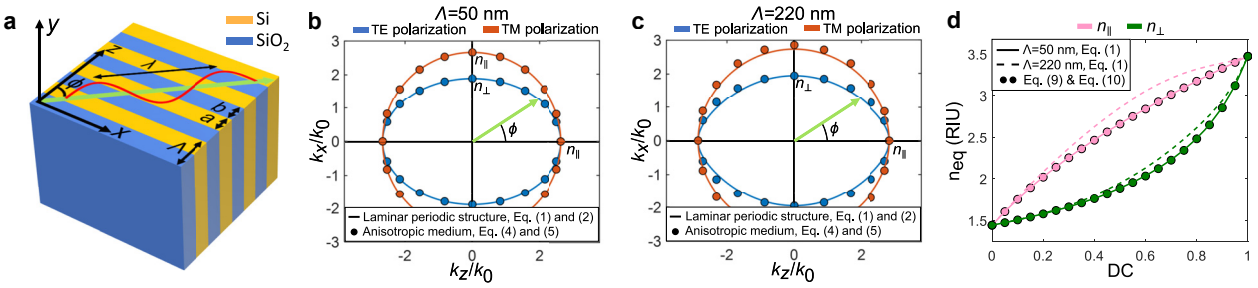

Figure 3: (a) Laminar periodic structure comprising two transversely infinite materials arranged along the *z*-axis with a period Λ. The laminae have lengths $a = \mathrm{DC}\cdot\Lambda$ and $b = (1-\mathrm{DC})\cdot\Lambda$, and refractive indices n_1 and n_2. (b), (c) Comparison between the normalized wave vector components, k_x and k_z, of a plane wave propagating along any angle of the laminar periodic structure (DC = 0.5) and of its equivalent anisotropic homogeneous material for the structure operating in the (b) long-wave regime, Λ = 50 nm, and (c) subwavelength regime, Λ = 220 nm. (d) Dependence with the duty cycle of the permittivity tensor components $n_\parallel$ and $n_\perp$ of the equivalent anisotropic homogeneous structure.

$$\frac{k_x^2}{n_\perp^2} + \frac{k_z^2}{n_\parallel^2} = k_0^2, \tag{4}$$

$$\frac{k_x^2}{n_\parallel^2} + \frac{k_z^2}{n_\parallel^2} = k_0^2. \tag{5}$$

Equations (4) and (5) are the dispersion relations of TE and TM plane waves propagating along the *x*–*z* plane of a uniaxial anisotropic crystal [43], with $n_\parallel$ and $n_\perp$ ordinary and extraordinary indices of refraction respectively. Note that Eq. (4) corresponds to an ellipse while Eq. (5) is a circle. That is to say, a plane wave propagating along a laminar periodic structure in the long wave regime behaves as if it propagated along a homogeneous uniaxial crystal defined by the diagonal permittivity tensor ε_1:

$$\boldsymbol{\varepsilon_1} = \begin{bmatrix} n_\parallel^2 & 0 & 0 \\ 0 & n_\parallel^2 & 0 \\ 0 & 0 & n_\perp^2 \end{bmatrix}. \tag{6}$$

The parameters $n_\parallel$ and $n_\perp$ are the effective indices of a TE plane wave propagating along the *z*-axis and the *x*-axis of the laminar periodic structure, respectively, and can thus be defined from Eq. (1) as

$$n_\parallel = k_z/k_0 \ (\text{when } k_x = 0), \tag{7}$$

$$n_\perp = k_x/k_0 \ (\text{when } k_z = 0). \tag{8}$$

In the Supplementary material we provide MATLAB and Python scripts to calculate the indices $n_\parallel$ and $n_\perp$. For the complete modeling of the metamaterial, we are only considering the equation for TE polarization [Eq. (1)], as it characterizes both required indices. Remarkably, the $n_\parallel$ parameter also yields a good description for TM polarization, because TM-polarized light is parallel to the laminae irrespective of the direction of propagation. In Figure 3(b) and (c) we compare the wave vector of a plane wave propagating along the laminar materials and along its equivalent anisotropic structure in the long-wave regime, Λ = 50 nm, and for a practical pitch, Λ = 220 nm, for DC = 0.5. In both cases, the pairs (k_x, k_z) are obtained from Eqs. (1) and (2) for the laminar periodic structure and from Eqs. (4) and (5) for the equivalent anisotropic medium.

In the long-wave regime [Figure 3(b)], the laminar SWG and its homogenized model exhibit the exact same behavior. Moreover, it can be shown that in this regime the metamaterial properties do not depend on the period nor the wavelength, allowing us to simplify the permittivity tensor components as [7]:

$$n_\parallel^2 \approx \mathrm{DC}\cdot n_1^2 + (1-\mathrm{DC})\cdot n_2^2, \tag{9}$$

$$n_\perp^2 \approx \left(\mathrm{DC}\cdot n_1^{-2} + (1-\mathrm{DC})\cdot n_2^{-2}\right)^{-1}. \tag{10}$$

As intuition predicts, a high duty cycle implies permittivity tensor components close to n_1 and a low duty cycle implies tensor components close to n_2 [see Figure 3(d)]. Indeed, this is the principle which enables refractive index engineering using subwavelength materials.

For the larger 220-nm pitch, the laminar periodic structure and the anisotropic metamaterial still yield a remarkably similar result, implying that the latter is a good model for the former even when the long-wave condition is not satisfied [see Figure 3(c)]. Even the duty-cycle dependence of $n_\parallel$ and $n_\perp$ closely follows the results obtained in the long-wave regime [see Figure 3(d)].

Having discussed the properties of infinite laminar materials, we return to our main goal: understanding to what extent subwavelength-patterned waveguides, such as those in Figure 4(a) and (e), can be modeled by homogeneous anisotropic metamaterial waveguides. For this purpose, the modes of the subwavelength waveguide have been calculated rigorously using a 3D finite-difference time-domain (FDTD) software for photonic

structures [44]. The parameters $n_{\parallel}$ and $n_{\perp}$ of the metamaterial waveguide have been calculated using the script given in the supplementary material. The modes of the resulting anisotropic waveguide were then obtained using a simple finite element method (FEM) mode solver for photonic structures [45].

Figure 4(b) compares the effective indices of the fundamental TE and TM modes of the longitudinal subwavelength waveguide [Figure 4(a)] with those of the metamaterial waveguide, as a function of the structural pitch. We observe that the laminar model yields a satisfactory estimation of the effective indices for both the fundamental TE and TM modes up to a pitch of ~200 nm. Beyond that point, the infinite laminar structure approaches its Bragg threshold $\Lambda_{\text{Bragg}}^{\text{lam}} = 240$ nm, and can no longer represent the subwavelength waveguide, which has a significantly larger Bragg threshold $\Lambda_{\text{Bragg}}^{\text{wg}} = 300$ nm. The propagation constants of higher-order modes are compared in Figure 4(c) and (d). As expected, in the long-wave limit ($\Lambda = 50$ nm) the anisotropic model is in very good agreement with the exact Floquet–Bloch solution. Remarkably, even for a comparatively large pitch of 220 nm, the anisotropic model provides a very good description of higher-order modes for both polarizations with a maximum error in the effective index below 6%.

Figure 4(f) compares the effective indices of the fundamental TE and TM modes of the transverse subwavelength waveguide [see Figure 4(e)] with those of the metamaterial waveguide, as a function of the structural pitch. We observe a very good agreement in the long-wave regime, with the results of the metamaterial waveguide becoming slightly less accurate as the pitch is increased. This mismatch is especially remarkable for the TM polarization, as it mainly depends on the $n_{\parallel}$ component of the tensor, which is the component affected by the Bragg regime. For the higher-order modes, the propagation constants are very well predicted in the long-wave regime [see Figure 4(g)] and exhibit an error below ~3% for a 220-nm pitch [see Figure 4(h)].

2.2 Slab material model

The main purpose of the slab material model is to overcome the limitations of the laminar model in the vicinity of the Bragg threshold. This is achieved by considering the silicon

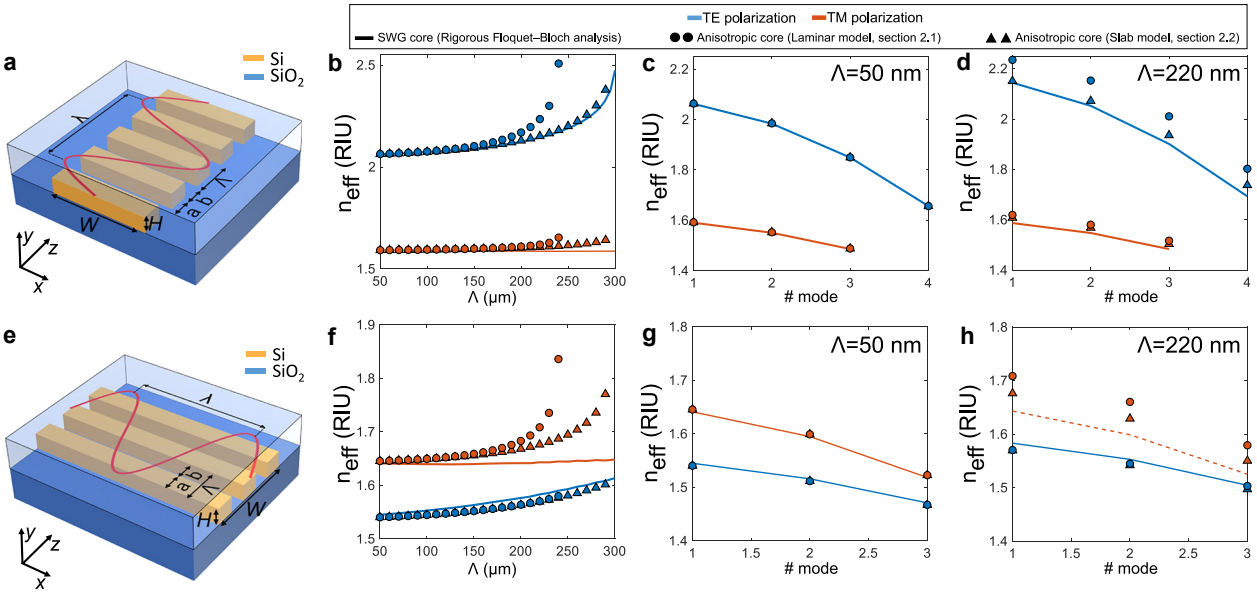

Figure 4: (a) Schematic representation of a longitudinal SWG waveguide. (b)–(d) Effective indices of (b) the fundamental Floquet–Bloch mode and (c), (d) higher order Floquet–Bloch modes of a longitudinal SWG waveguide calculated by rigorous 3D full-vectorial simulations (TE: Blue solid lines, TM: Orange solid lines) compared with those of the corresponding anisotropic homogeneous-core waveguides obtained using the laminar model (circles) and the slab model (triangles). (e) Schematic representation of a transverse SWG waveguide. (f)–(h) Effective indices of (f) the fundamental Floquet–Bloch mode and (g), (h) higher order Floquet–Bloch modes of a transverse SWG waveguide calculated by rigorous 3D full-vectorial simulations (TE: Blue solid lines, TM: Orange solid lines) compared with those of the corresponding anisotropic homogeneous-core waveguides obtained using the laminar model (circles) and the slab model (triangles).

thickness H as a parameter of the material itself [see Figure 5(a)]. Following a similar argument as in the previous section, we calculate the permittivity tensor components from the propagation of two TE-polarized plane waves propagating along the x- and the z-axis. As opposed to the laminar model, for which analytical formulas are available, these calculations have to be performed numerically. Using the slab model is still advantageous over the rigorous 3D Floquet–Bloch analysis of the subwavelength-structured waveguide, because the calculations required for the model can be performed very efficiently using 2D plane-wave expansion method simulations [46]. As a result, we obtain the effective indices of the fundamental TE slab mode propagating along the z- and the x-axis, n_{eff_x} and n_{eff_z} [see Figure 5(b)]. Here the subindices indicate the polarization and not the direction of propagation. In order to convert these effective indices into refractive indices describing the metamaterial, we solve an isotropic slab for different core material refractive indices n_{eq}, obtaining the mapping function shown in Figure 5(c). Finally, we map the effective indices n_{eff_x} and n_{eff_z} into the equivalent refractive indices n_{eq_x}, and n_{eq_z} shown in Figure 5(d).

These parameters are analogous to $n_{\parallel}$ and $n_{\perp}$ from Section 2.1, i.e., the metamaterial can be modeled as

$$\boldsymbol{\varepsilon}_s = \begin{bmatrix} n_{\mathrm{eq}_x}^2 & 0 & 0 \\ 0 & n_{\mathrm{eq}_x}^2 & 0 \\ 0 & 0 & n_{\mathrm{eq}_z}^2 \end{bmatrix}. \tag{11}$$

From Figure 4(b) it is apparent that the slab model is indeed more accurate than the laminar model in the vicinity of the Bragg threshold, yet at the expense of a higher complexity in the modeling stage. This improvement is also seen when higher-order modes are considered: while for the 50-nm pitch both laminar and slab models give virtually exact results [see Figure 4(c)], for the 220-nm pitch the error in the effective indices is below 3% for the slab model, compared to 6% for the laminar approximation [see Figure 4(d)]. Regarding the transverse subwavelength waveguide, the slab model does also provide benefits compared to the laminar model [see Figure 4(f)–(h)].

The homogenization technique described above can be also applied when structural parameters of the subwavelength structure gradually change in the transverse direction. The subwavelength waveguide works then as a GRIN metamaterial described by a tensor $\varepsilon(x)$, that is locally defined by a structural apodization function. Figure 6(a) and (d) show two representative examples where the duty cycle changes along the transverse direction, being DC(x) the subwavelength apodization function [see Figure 6(b) and (e)] [32, 47]. In Section 4 we describe the design process of an ultracompact SWG-assisted GRIN-lens spot size converter.

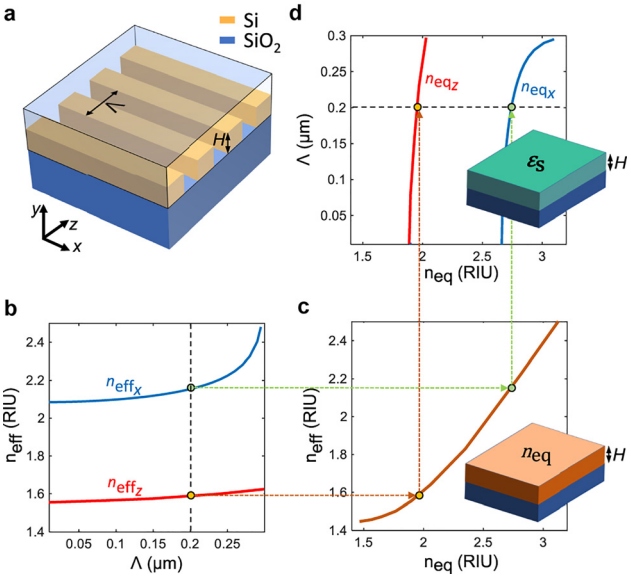

Figure 5: (a) Subwavelength grating slab with periodic core of period Λ and silicon thickness $H = 220$ nm. (b) Effective index of the fundamental TE slab mode propagating along the z-axis (n_{eff_x}) and x-axis (n_{eff_z}). (c) Mapping function between the effective index of the fundamental TE mode of an isotropic slab and the corresponding core material refractive index. (d) Synthesized refractive index tensor components for a periodic-core slab with period Λ.

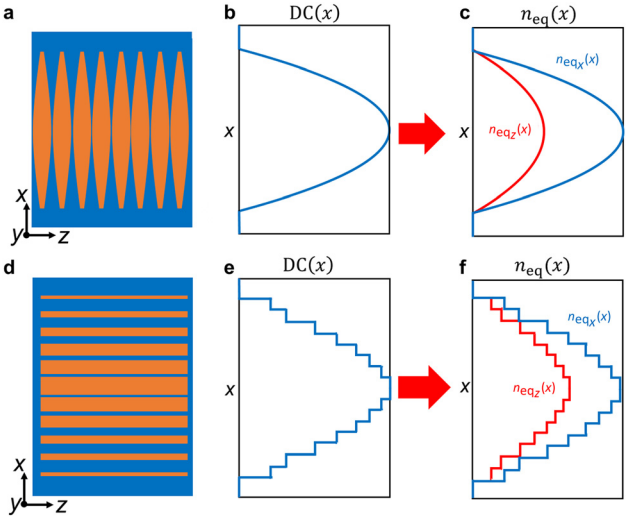

Figure 6: GRIN metamaterial waveguides with variable duty cycle based on (a) longitudinal and (d) transverse SWG structures. (b), (e) Apodized duty cycle DC(x) of the subwavelength structures in (a) and (d), respectively. (c), (f) Homogeneous anisotropic metamaterial tensor components $n_{\mathrm{eq}_x}(x)$ and $n_{\mathrm{eq}_z}(x)$ of the subwavelength structures of (a) and (d), respectively.

2.3 Controlling birefringence with tilted subwavelength waveguides

So far, we have discussed how the longitudinal and transverse subwavelength waveguides shown in Figure 4(a) and (e) can be modeled using an anisotropic metamaterial core defined by the permittivity tensor $\boldsymbol{\varepsilon} = \mathrm{diag}[n_{xx}^2, n_{yy}^2, n_{zz}^2]$. In anisotropic materials, the behavior of light waves depends on the orientation of the electric field components with respect to the optical axis of the material. Therefore, the idea of tilting the anisotropic subwavelength structure to control the light propagation through a waveguide naturally emerges. Figure 7(a) shows a schematic of a silicon SWG waveguide in which the core segments have been tilted by an angle θ. Under the validity conditions of the discussed laminar (Section 2.1) and slab (Section 2.2) models, the core material of the tilted SWG waveguide core can be approximated by the permittivity tensor $\tilde{\boldsymbol{\varepsilon}}$ [48]:

$$\tilde{\boldsymbol{\varepsilon}} = \mathbf{T}^{-1}\boldsymbol{\varepsilon}\mathbf{T} = \begin{bmatrix} \tilde{n}_{xx}^2(\theta) & 0 & \tilde{n}_{xz}^2(\theta) \\ 0 & \tilde{n}_{yy}^2(\theta) & 0 \\ \tilde{n}_{xz}^2(\theta) & 0 & \tilde{n}_{zz}^2(\theta) \end{bmatrix}, \tag{12}$$

where $\mathbf{T}$ is the rotation matrix in the x–z plane and θ is the tilt angle of the SWG segments.

The different elements of the tensor are given by

$$\begin{aligned} \tilde{n}_{xx}^2 &= n_{xx}^2\cos^2(\theta) + n_{zz}^2\sin^2(\theta), \tilde{n}_{yy}^2 = n_{yy}^2, \\ \tilde{n}_{zz}^2 &= n_{xx}^2\sin^2(\theta) + n_{zz}^2\cos^2(\theta), \\ \tilde{n}_{xz}^2 &= (n_{zz}^2 - n_{xx}^2)\cos(\theta)\sin(\theta). \end{aligned} \tag{13}$$

Note that the $\tilde{n}_{yy}$ component of the tensor does not change with the tilt angle. Therefore, this structure enables direct control over modal birefringence, only by changing the tilt angle θ, while using a constant duty cycle. This is illustrated in Figure 7(b), where we study the effective index of the fundamental TE and TM modes of the longitudinal SWG waveguide studied in Figure 4 with the tilt angle, using the slab model from Section 2.2. It is observed that the fundamental TE mode is strongly affected by the rotation angle, while the TM is virtually unaffected. These results are accurately predicted by the anisotropic metamaterial described by the tensor in Eq. (12). This control over the birefringence makes tilted SWGs ideal structures for the design of polarization management devices.

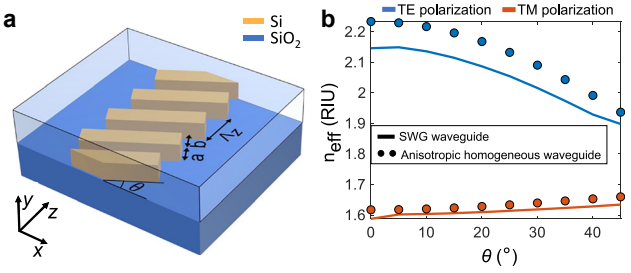

Figure 7: (a) Schematic representation of a tilted SWG waveguide. The period of the structure, $\Lambda_z = \Lambda/\cos(\theta)$, is much shorter than the wavelength, λ, of the light propagating along the z-axis. (b) Effective index of the fundamental TE and TM modes of the tilted subwavelength waveguide and the anisotropic homogeneous waveguide.

3 SWG-based devices

This section provides a thorough review of the state of the art in the application of subwavelength structures to integrated optical devices. We give insight into the operation of each of the devices and provide a detailed comparison of their performance. This article gathers the state of the art from 2018 onward, thereby complementing our previous reviews [18, 40, 41].

3.1 Ultralow loss waveguide crossings and bends

Low-loss and low-crosstalk waveguide bends and crossings are essential structures needed for dense integration. The main problem in waveguide bends is the optical length difference between the inner and the outer edges of the waveguide. This difference not only causes a mode mismatch between the modes of the straight and the curved waveguides but also produces intermode crosstalk. Subwavelength grating metamaterials have demonstrated to solve both problems by compensating the optical path difference via refractive index engineering. This compensation can be done using SWG structures with trapezoidal shape inside the curve [49, 50] [See Figure 8(a) and (b)] or tapered before and after the curve [51] [See Figure 8(c)]. The reduction on the bending loss of trapezoidal SWG allows to increase the Q-factor of SWG-based ring resonators by a factor between 3 and 5, compared to non-trapezoidal SWG bends [49]. Moreover, the mode shape adaptation allowed by SWG structures has enabled waveguide bends supporting up to four modes with a crosstalk lower than –20 dB, more than 10 dB lower than conventional multimode bends. In a non-optimized waveguide crossing, high insertion loss and crosstalk are a result of the transition between high-index-contrast waveguides, in which the mode field is

highly confined, and the intersection zone, with no index contrast (free space). This discontinuity generates back-reflections and scattering into the perpendicular waveguides. Subwavelength grating structures reduce the index contrast, thereby smoothing the transition between the waveguides and the intersection zone and reducing the insertion loss and crosstalk (IL < 0.02 dB/crossing, CT < –40 dB) [52]. Graded-index devices [53], such as Luneberg lenses [54], constitute another interesting approach to design crossings. While these components have been demonstrated using periodic nanorods, the use of subwavelength-grating structures as those covered in this review paper would help shorten the device length by harnessing their anisotropic properties [32]. Implementing such GRIN material without SWG requires complex nonstandard fabrication method such as grayscale lithography [55].

3.2 Broadband beam splitters and phase shifters

On-chip beam splitters are fundamental building blocks for almost any photonic integrated circuit, where they are often used cascaded and combined with other devices to perform complex functions. As such, their performance, both in terms of insertion losses and imbalance, as well as phase error between the outputs, is crucial. Additionally, broad bandwidths or the ability to handle multiple modes are becoming increasingly important [56, 57]. The properties of subwavelength structures can be exploited in combination with a variety of beam splitter configurations, illustrated in Figure 9, to enhance their functionality. In the following, we will be focusing on 50/50 splitters, as these are arguably the most widely used. For detailed performance information about the different splitters, the reader is referred to Table 1.

In a Y-branch [Figure 9(a)] the input waveguide is gradually split in two, so that the input mode, φ_{in}, smoothly evolves into the even super-mode of the two output waveguides, φ_{even}; consequently, Y-branches exhibit no imbalance. One of the main drawbacks of this configuration is the sharp tip of the gap between the output waveguides, which is challenging to fabricate and can lead to performance degradation. Using inversely tapered waveguides with subwavelength structures between them, an ultracompact, polarization insensitive Y-branch has been recently proposed in Ref. [58]. Another approach is to substitute the gap between the waveguides by an array of subwavelength holes that adiabatically increase in size [59] thus synthesizing a metamaterial with a gradually decreasing equivalent index. This enables the implementation of a Y-branch that can operate up to the fourth mode with the remarkable performance shown in Table 1.

Adiabatic couplers, shown schematically in Figure 9(b), consist of waveguides that are tapered in width, thereby smoothly transforming the mode of the wide input waveguide, $\varphi_{in,1}$, into the even supermode at the output, φ_{even}, and the mode of the narrow input waveguide, $\varphi_{in,2}$, into the odd supermode at the output, φ_{odd}. This adiabatic transformation is demonstrated with measured bandwidths of almost 400 nm for both polarizations in Ref. [60], without using subwavelength structures. Typically, rather long devices are required to ensure adiabaticity. One way to overcome this issue is using a bent geometry to suppress undesired coupling and achieve a measured imbalance of only 0.12 dB [61]. Subwavelength structures provide another alternative to achieve shorter structures, by either lowering the equivalent index of the waveguides, or increasing the equivalent index of the gap between them [62, 63]. Using both approaches, devices with excellent performance in bandwidths exceeding 100 nm have been demonstrated.

Directional couplers [Figure 9(c)] exchange power between adjacent waveguides via the constructive and

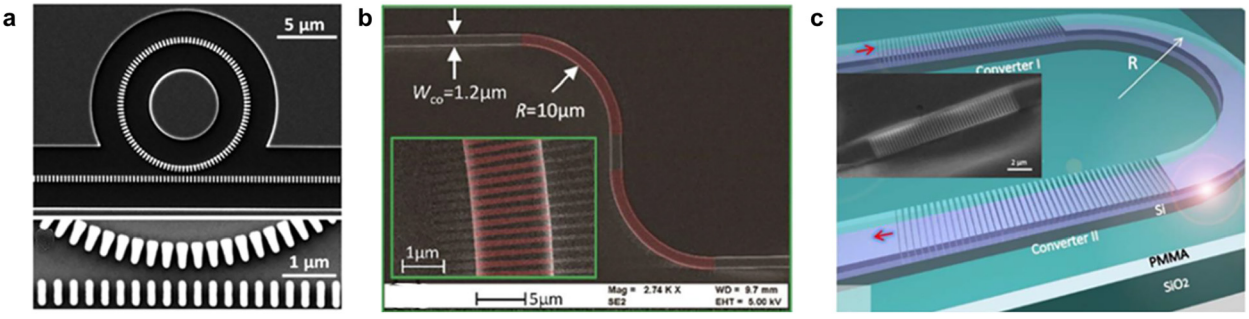

Figure 8: (a), (b) Trapezoidal SWG structures inside the bend and (c) tapered SWG structures before and after the bend to compensate the lateral shift of the mode. Reproduced with permission from Refs. [49–51].

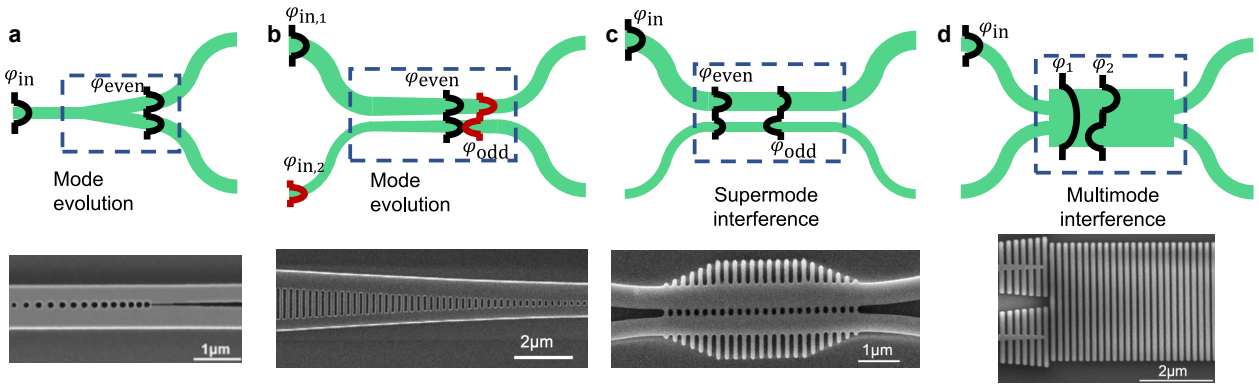

Figure 9: Configurations of conventional beam splitters and scanning electron micrographs of exemplary subwavelength implementations: (a) Y-branch, (b) adiabatic coupler, (c) asymmetric directional coupler, and (d) multimode-interference coupler. These devices exploit subwavelength structures to achieve smaller size, better performance, or both. Micrographs in (a), (b), and (c) are reproduced with permission from Refs. [59, 63, 65].

Table 1: Performance comparison of recently demonstrated subwavelength-enhanced on-chip beam splitters. All devices operate at near-infrared wavelengths.

Ref.	Configuration	Pol.	# modes	Simulation			Experiment			Length
				IL (dB)	IB (dB)	BW (nm)	IL (dB)	IB (dB)	BW (nm)	(μm)
[62]	2 × 2 adiabatic coupler	TE only	1	0.2	1	500	0.1	0.3	185	35
[63]	2 × 2 adiabatic coupler	TE only	1	0.2	1	600	0.2	0.3	100	65
[70]	1 × 2 inverse design	TE and TM	1	0.5	–	80	1	–	80	2.4
[58]	1 × 2 Y-branch	TE and TM	1	0.2	–	400	–	–	–	3
[67]	1 × 2 slotted MMI	TE and TM	1	0.3	–	200	–	–	–	4
[59]	1 × 2 Y-branch	TE only	4	0.1	–	100	0.5	–	40	29
[69]	2 × 2 thin film interference	TE only	3	0.5	<1	415	–	–	–	315
[64]	2 × 2 symmetric DC	TE only	1	0.6	0.6	100	–	–	–	
[65]	2 × 2 asymmetric DC	TE only	1	0.4	0.3	300	1	0.5	200	6
[30]	2 × 2 anisotropic MMI	TE only	1	1	0.5	500	1	1	300	25
[60][a]	1 × 2 adiabatic coupler	TE and TM	1	0.1	<0.1	500	1	1	390	200
[61][a]	2 × 2 adiabatic coupler	TE only	1	0.1	0.4	400	0.5	0.1	145	31

[a]Non-SWG devices, included for reference. IL, Insertion Loss; IB, Imbalance; BW, Bandwidth.

destructive interference of their supermodes, so that the beat length $L_\pi = (\lambda_0/2)/(n_{\text{eff,even}} - n_{\text{eff,odd}})$ dictates the device length. In conventional devices, this beat length is strongly wavelength-dependent, which ultimately limits the bandwidth. For symmetrical directional couplers with 50/50 splitting, we proposed in Ref. [64] the superposition of a longitudinal subwavelength structure in the coupling region, to engineer modal dispersion and flatten the beat length. For 50/50 splitting, a judiciously designed asymmetric directional coupler exhibits an intrinsically larger bandwidth, which, when combined with subwavelength dispersion engineering, results in very large bandwidth: a measured bandwidth of 200 nm with very good performance was demonstrated in Ref. [65].

In multimode interference (MMI) couplers [Figure 9(d)], images of the input field are formed at distances governed by the beat length. In Ref. [30] we showed that an MMI comprising a longitudinal subwavelength structure exhibits a wide bandwidth which is a direct consequence of the metamaterial anisotropy. For an MMI of width W_{MMI} the beat length is approximately given by $L_\pi^{\text{aniso}} = (4W_{\text{MMI}}/3)((1/\lambda_0)(n_\perp^2/n_\parallel))$, and the wavelength dependence of the term $n_\perp^2/n_\parallel$ can practically cancel the term $1/\lambda_0$. On the other hand, MMIs with subwavelength holes arrayed along the propagation direction have been shown to reduce device length by a factor of two [66]. This concept has been extended to an ultrashort device capable of handling both TE and TM polarization [67].

More recently, it has been shown that material anisotropy can also be exploited in phase shifters to achieve ultrabroadband operation [68]. As an example, consider a conventional phase shifter composed of two

waveguide arms of different widths as shown in Figure 10. The modes φ_A and φ_B propagating through these waveguides exhibit different effective indices and thus accumulate a differential phase shift $\Delta\theta = (2\pi/\lambda_0)(n_{\text{eff,A}} - n_{\text{eff,B}})L$. This phase shift is, however, strongly wavelength dependent. In Ref. [68] it was shown that if wide subwavelength waveguides are used in both arms the phase shift is approximately given by $\Delta\theta = (\pi/4)(1/W_B - 1/W_A)(\lambda_0(n_\parallel/n_\perp^2))$, and as in the case of the SWG MMI, the wavelength dependence of the term $n_\parallel/n_\perp^2$ can be designed to cancel the term λ_0. An operational bandwidth of 400 nm was predicted by simulation, and a four-fold reduction of the phase error compared to a conventional phase shifter was experimentally demonstrated over a 145-nm bandwidth.

Subwavelength structures have also been successfully used in less conventional device configurations. In Ref. [69], a splitter capable of operating with three modes in a bandwidth in excess of 400 nm is proposed by exploiting a subwavelength-engineered thin film effect. An ultracompact inverse design splitter that handles both TE and TM polarization has been demonstrated in Ref. [70], achieving subdecibel losses over an 80-nm bandwidth.

3.3 On-chip beam shaping

On-chip beam manipulation has multiple applications including feeding of surface grating couplers [13, 71–73], environmental monitoring and security [74], on-chip particle acceleration [75], or wavelength demultiplexing [76]. Spot size conversion is arguably the most common beam shaping operation. For instance, beam expansion is required to transfer light from narrow Si-wire interconnecting waveguides to wide surface grating couplers. This operation is traditionally tackled by means of adiabatic transitions that smoothly change the width of the waveguide. This approach, however, requires a large footprint to ensure a virtually lossless adiabatic transition. Recently, several SWG-engineered devices that achieve efficient beam expansion in a compact footprint have been reported. Most of them implement a planar lens by either using subwavelength structures to realize a GRIN waveguide or tailoring the local phase front of an incident beam. In Ref. [32], a beam expander has been proposed using a wide SWG-based GRIN waveguide in which the duty cycle varies transversally to synthesize a parabolic index profile [see Figure 11(a)]. This GRIN waveguide behaves like a conventional lens that generates a collimated and expanded image of the incident beam at the focal length. The fabricated device achieves wideband (BW > 130 nm) and efficient (IL < 1 dB) 30-fold beam expansion in a tenth of the footprint of an optimized adiabatic taper that exhibits similar loss [77]. The design process of this SWG-based GRIN lens will be covered in Section 4 using the anisotropic properties of SWGs. A 4-f-system beam expander for multiple modes has been demonstrated in Ref. [78] by combining two SWG-based lenses, as shown in Figure 11(b). The lenses were implemented by varying the width of longitudinal silicon strips, achieving compact and efficient 5-fold expansion even for arbitrary field profiles. An insertion loss of ~1.5 dB was experimentally shown, while the back-to-back inter-modal crosstalk of two devices was lower than −7 dB in a bandwidth of 25 nm.

A different way to achieve beam focusing relies on metasurface-like phase-front shaping. In Ref. [79], subwavelength patterning of slots in a silicon slab was successfully used to locally control the phase front of a collimated incident beam, so that the fundamental mode of a wide waveguide (11 μm) is focused on to a narrow waveguide (500 nm) in a short length of 13.7 μm. The demonstrated device, shown in Figure 11(c), exhibited low loss (IL < 1 dB) over a broad bandwidth (BW > 200 nm).

The beam shape can also be controlled by means of on-chip deflectors. A deflector is a grating waveguide that progressively diffracts the guided light towards a slab, thereby maintaining the light confined within the chip plane, as shown in Figure 12. By properly apodizing the grating strength, any arbitrary field profile can be formed in the slab region, while the phase front can be tuned by chirping the period of the structure. This concept has been exploited in Ref. [80], using an SWG slab to mitigate the inherent off-chip radiation of diffractive gratings. The deflector achieved an extreme beam expansion (×70) from

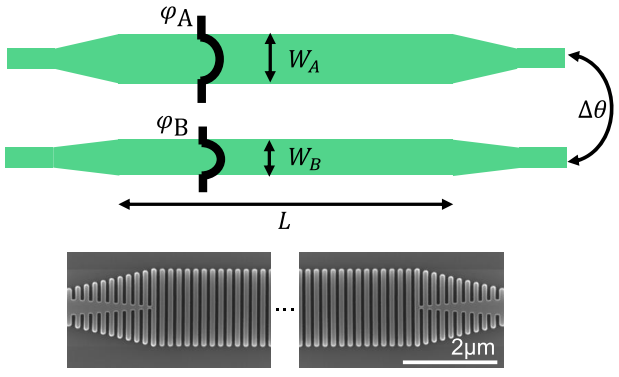

Figure 10: (a) Conventional phase shifters use waveguides of different widths to achieve a controlled phase shift $\Delta\theta$ between them. When these waveguides are substituted by subwavelength structures the operational bandwidth of the phase shifter can be extended by a factor of four.

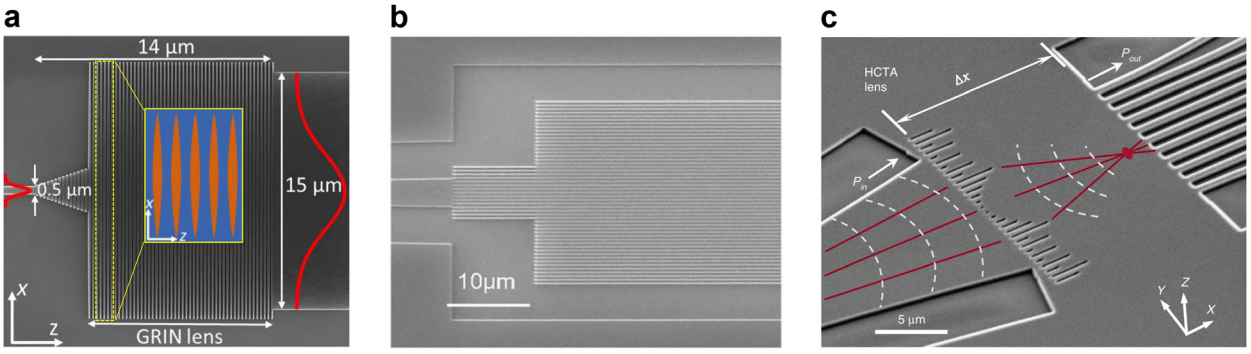

Figure 11: On-chip integrated lenses implemented with SWG structures.
(a) GRIN-lens spot size converter [32]. (b) 4-f system comprising two GRIN lenses using a subwavelength stacking of silicon strips [78]. (c) On-chip lens using a subwavelength single-layer high-contrast transmit array metasurface [79]. Reproduced with permission from Refs. [32, 78, 79].

the fundamental mode of a standard silicon wire to a collimated Gaussian beam in a compact footprint of 100 µm × 5 µm. By judicious grating pitch design and SWG index engineering, off-chip radiation from the deflector can be completely eliminated [81]. To achieve a similar effect without SWG structures it is necessary to use either a third material with a refractive index ~2.5 or multiple etch depths. Both strategies greatly complicate the fabrication compared with the SWG-based slab.

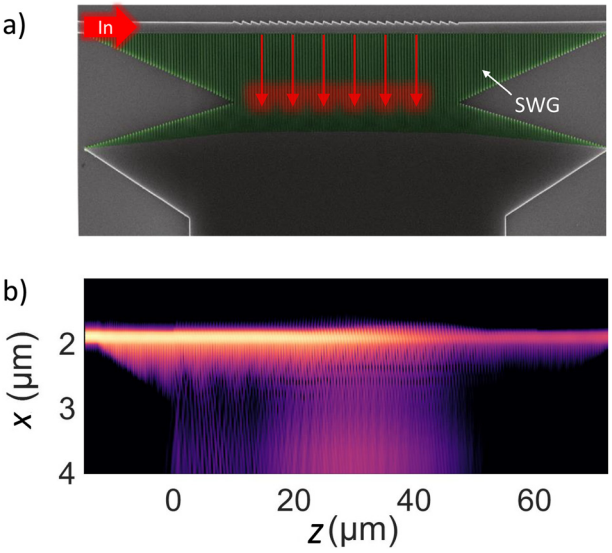

Figure 12: (a) SEM image of a fabricated sidewall grating deflector. The red arrows indicate the deflected light propagation direction and the green region comprises the SWG. (b) Field propagation inside the deflector. The light entering from the left gets progressively diffracted towards the wide waveguide as a collimated Gaussian beam.

3.4 Polarization management devices

Photonic integrated devices in silicon platforms often exhibit strong polarization dependence. This is due to the asymmetrical aspect ratio of the waveguide cross-section, the submicron scale of the waveguides, and the high index contrast of the materials. However, polarization independence is often desired because optical fibers randomly change the polarization state of the light to be injected into the chip. This can be achieved by using either polarization-diversity components – including polarization beam splitters (PBS), polarization rotators (PR), and polarization filters (PF) – or polarization-independent devices *per se*. Subwavelength engineering provides new degrees of freedom to tackle the design of both families of devices. It has to be highlighted that the operation of many of the devices discussed here only becomes possible as a result of the unique properties of subwavelength structures.

3.4.1 Polarization controlling devices

In the following, we discuss the latest SWG-based polarization management devices. They can be used for both polarization-diversity and polarization-division multiplexing (PDM) schemes. For a summarized perspective, we refer the reader to Table 2.

In polarization beam splitters, horizontally and vertically polarized modes in the input waveguide are separated into two independent output ports [see Figure 13(a)]. A typical configuration is the asymmetric directional coupler, composed of two parallel waveguides with different optical properties. Subwavelength grating structures can be used to ensure that the phase matching condition is satisfied for a

Table 2: Performance comparison of recently demonstrated subwavelength-enhanced polarization beam splitters.

Ref.	Device	Operation principle	Platform (Si thickness H)	Length	Simulation		Experimental	
					Max. IL (dB) @ BW (nm)	Min. ER (dB) @BW (nm)	Max. IL (dB) @ BW (nm)	Min. ER (dB) @ BW (nm)
[82]	PBS	Bridged DC	340 nm	6 μm	0.63@100	20@60	–	–
[83]	PBS	DC	220 nm	7.2 μm	1@180	10@170	2.5@150	10@150
[84]	PBS	Tilted DC	220 nm	14 μm	1@100	20@86	1@143	15@72
[85]	PBS	Tilted DC	340 nm	7.5 μm	0.6@60	20@75	–	–
[86]	PBS	Skin-depth DC	300 nm*55 nm of SiO_2 sandwiched in core	9.91 μm	0.4@100	20@50	–	–
[87]	PBS	Cascaded skin-depth DC	220 nm	130 μm	0.4@250	20@250	–	–
[88]	PBS	MMI	220 nm	133 μm	1.15@95	20@110	2.5@84	11.7@84
[89]	PBS	Tilted SWG MMI	220 nm	118 μm	1@131	20@131	–	–
[90]	PBS	Tilted SWG MMI	220 nm	118 μm	1.6@130	20@130	1@120	13@120
[31]	PBS	Skin-depth MMI	250 nm	12.3 μm	1@200	20@210	<1@200	>20@200
[92]	PBS	Mode evolution	340 nm	76.8 μm	0.3@270	20@270	1@230	20@240
[93]	PR	Hybridized structure	340 nm	4.8 μm	1@415	20@415	–	–
[94]	PSR	Mode evolution	220 nm	171 μm	0.5@120	15@120	1.4@90	15@105
[94]	PSR	Mode evolution	220 nm*90 nm shallow etched	185 μm	0.5@120	15@120	1.4@120	15@120
[95]	PF	Skin-depth cladding	250 nm	13 μm	1@415	25@415	1@415	20@415
[96]	PF	Birefringence engineering	250 nm	56 μm	1@210	36@210	–	–

single polarization, so that only one of the input modes couples to the cross output. Multiple polarization-splitting asymmetric directional couplers have been recently demonstrated that use longitudinal [82, 83] and tilted SWG structures [84, 85]. The latter are especially interesting, as they can break the waveguide symmetry by simply tilting the core segments [see Figure 13(a.i)]. Another alternative to design directional coupler polarization beam splitters is by using skin depth engineering [33]. The evanescent field decay is controlled to isolate both arms of the directional coupler for the TE polarization, allowing the cross-coupling for the TM mode [86]. This device can be cascaded multiple times, improving their performance [87]. MMI couplers are also commonly used for polarization beam splitting. Compared with directional couplers, MMIs have larger bandwidths, tolerance to fabrication errors, and extinction ratio, yet at the expense of a larger footprint. In MMI devices, the images of the input fields are formed at different output ports [see Figure 13(a.ii)] for each polarization. SWG structures enable the birefringence engineering needed to tune the beat lengths for each polarization [88–90]. The birefringence engineering can be tuned either by tuning the period of the structure [88] or the tilt angle of the silicon segments [89, 90]. Dai et al. use SWG-enabled skin-depth engineering to achieve conventional MMI behavior for the TM polarization while the PBS acts like two uncoupled waveguides for the TE polarization [see Figure 13(a.iii)], experimentally demonstrating an outstanding performance, IL < 1 dB, ER > 20 dB over a bandwidth of 210 nm [31]. The operation of this device will be analyzed in more detail in Section 4. Furthermore, the control of SWG metamaterials over the effective indices of the modes and the polarization birefringence is especially convenient for mode-evolution devices [91]. Recently, mode-evolution-based polarization beam splitting has been reported with excellent performance [92].

In polarization rotators, the input light is rotated into the orthogonal polarization state [see Figure 13(b)]. A polarization rotator (PR) and a polarization beam splitter (PBS) can be combined in a polarization beam splitter and rotator (PSR), which splits the input polarizations in two and then rotates the polarization state of one of outputs. Both PR and PSR are commonly implemented by exciting and beating hybrid modes or by using mode-evolution techniques. In hybrid-mode devices, the geometrical symmetry is broken [See Figure 13(b.i)] and the conversion length is typically highly wavelength-dependent. SWG structures enable broadband operation by engineering the

metamaterial dispersion and flattening the conversion length response with the wavelength [93]. In mode-evolution devices, on the other hand, the effective index and polarization birefringence engineering helps design adiabatic transitions that gradually rotate the polarization states [See Figure 13(b.ii)] [94].

Polarization filters suppress only one of the input polarization components [see Figure 13(c)]. These devices are important because polarization beam splitters or rotators with ideal performance in terms of extinction ratio are not available, and pure polarization excitation is not achievable. Integrated polarization filters are based on the leakage or the reflection of the undesired polarization, while allowing the other to propagate. In Ref. [95] the authors add a transverse SWG structure to the outside lateral cladding of a bent waveguide core [See Figure 13(c.i)], the TE mode is laterally confined due to the skin depth effect, while the TM mode is completely radiated to the adjacent SWG metamaterial region. In Ref. [96], by leveraging the intrinsic birefringence of the silicon-on-insulator (SOI) platform and by engineering the refractive index, an SWG waveguide is designed that only supports TE modes [See Figure 13(c.ii)].

3.4.2 Polarization-independent devices

Subwavelength gratings enable the design of polarization-insensitive devices. There is not a generic design method to achieve polarization-insensitivity devices, but it depends on the particular device. In interference-based devices such as DCs or MMIs, SWG structures have enabled polarization independency by properly tuning the beat lengths of both polarizations (birefringence engineering) [67, 97–99]. In mode-evolution devices, SWG structures produce smooth transitions and can be designed for both polarizations simultaneously [58]. Likewise, in grating couplers, SWG segmentation can be used to properly adjust the radiation angle for both polarizations [100, 101]. Most of these designs rely on the chirping of the duty cycle of the periodic structure, affecting both polarizations simultaneously [see Figure 3(d)]. In this context, tilted SWG

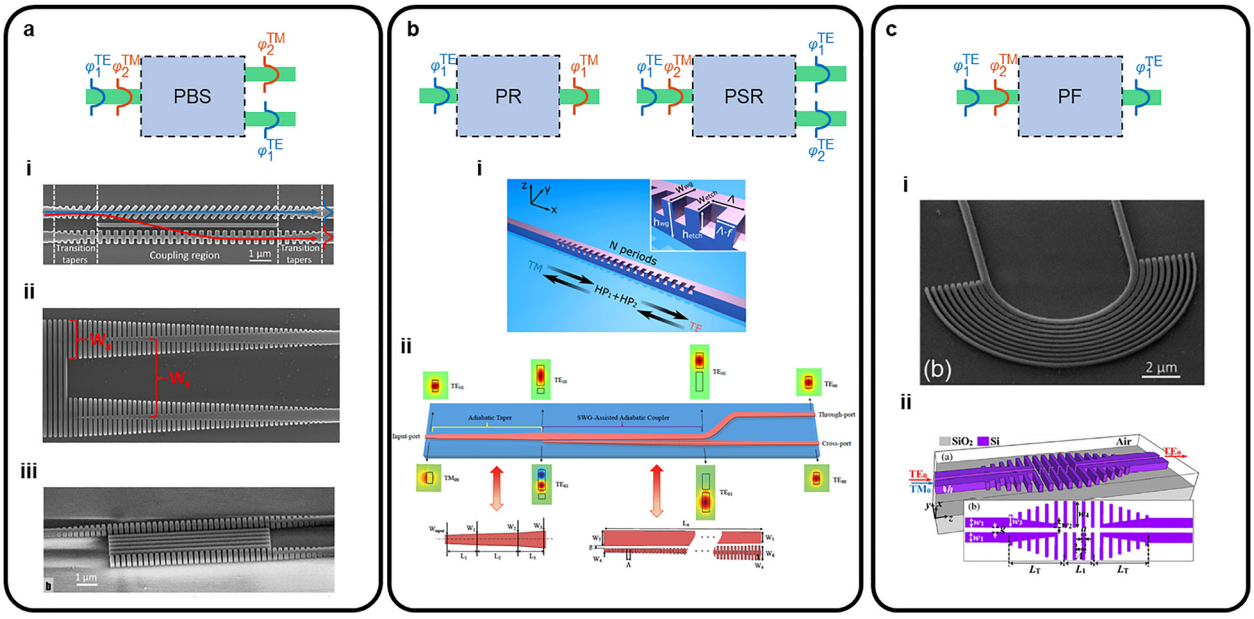

Figure 13: Configurations of polarization controlling devices.
(a) Polarization beam splitters: a.i) Tilted directional coupler, reproduced with permission from Ref. [84]; a.ii) birefringence-engineered MMI, reproduced with permission from Ref. [88]; and a.iii) skin-depth-engineered MMI, reproduced with permission from Ref. [31]. (b) Polarization rotators and polarization beam splitter and rotators: b.i) Hybrid waveguide with refractive index and dispersion engineering, reproduced with permission from Ref. [93] and b.ii) mode-evolution splitter and rotator, reproduced with permission from Ref. [94]. (c) Polarization filters: c.i) Cladding anisotropy-engineered curve, reproduced with permission from Ref. [95] and c.ii) refractive-index-engineered waveguide, reproduced with permission from Ref. [96].

structures are auspicious topologies, as they mainly affect the TE polarization with virtually no effect on TM modes [see Figure 7(b)], thus facilitating the design of polarization-agnostic devices. To date, these advanced structures have been used to design a nonbirefringent waveguide [102]. However, we foresee an increase in the utilization of these subwavelength structures in more complex optical devices.

3.5 Narrowband spectral filtering devices

A Bragg grating is a periodic structure that works as a frequency-selective distributed mirror, providing a high reflectivity within a specific spectral band around the Bragg wavelength λ_B, and transmitting the light at other wavelengths. In its basic form, an integrated Bragg reflector comprises a conventional waveguide with a periodic perturbation in either the composing material or the waveguide geometry. The reflection wavelength response of a canonical Bragg filter with period Λ_B and length $L = N\Lambda_B$ can be described using the following three parameters [103, Ch. 7]

(i) Central wavelength:

$$\lambda_B = 2n_F\Lambda_B, \tag{14}$$

(ii) Peak reflectance:

$$|r(\lambda_B)|^2 = |r|^2_{max} = \tanh^2(\kappa L) \xrightarrow{\kappa L \gg 1} |r|^2_{max} \simeq 1, \tag{15}$$

(iii) Full bandwidth between nearest nulls:

$$\Delta\lambda = \frac{\lambda_B^2}{Ln_g}\sqrt{1+\left(\frac{\kappa L}{\pi}\right)^2} \xrightarrow{\kappa L \gg 1} \Delta\lambda \simeq \frac{\lambda_B^2}{\pi n_g}\kappa, \tag{16}$$

where n_F is the effective index of the Floquet–Bloch mode supported by the grating, n_g is the group index of the unperturbed waveguide, and κ is the coupling coefficient between the forward and backward propagating modes. Since the coupling coefficient increases with the perturbation strength, Eq. (16) shows that Bragg filters with subnanometer bandwidth require weak perturbations.

An interesting approach to implement integrated Bragg filters is introducing a lateral corrugation on the waveguide sidewalls. Due to the high index contrast of the SOI platform, corrugations smaller than 10 nm are required to achieve bandwidths below 1 nm [104]. The need for such small corrugations in silicon waveguides hinders the practical implementation of narrowband, high-rejection SOI filters. Various narrowband integrated Bragg filters based on SWG waveguides have been proposed to overcome the drawbacks of conventional devices [28, 105–113]. In all cases, the filter is composed of a basic cell, of length Λ_B, that is divided into two SWG sub-periods of lengths Λ_1 and $\Lambda_2 = \Lambda_B - \Lambda_1$. The desired weak perturbation is induced in the structural configuration of the second sub-period.

Figure 14(a) schematically shows the SWG-assisted Bragg grating topology proposed by Wang et al. [105, 106]. In this case, $\Lambda_1 = \Lambda_2 = 0.5{\cdot}\Lambda_B$, and the only difference between the sub-periods is the duty cycle ($DC_1 = a_1/\Lambda_1 \neq DC_2 = a_2/\Lambda_2$). The authors report a measured 3-dB bandwidth of ~0.5 nm and a peak reflectivity of 94.4% for a filter length of 1.12 mm [106].

In Ref. [107], Perez-Galacho et al. proposed an SWG-based Bragg filter with a small variation in the corrugation width of the perturbed subperiods [see Figure 14(b)]. The perturbation strength depends on the difference between the successive corrugation widths ΔW and not on their absolute values. Double-width corrugation Bragg

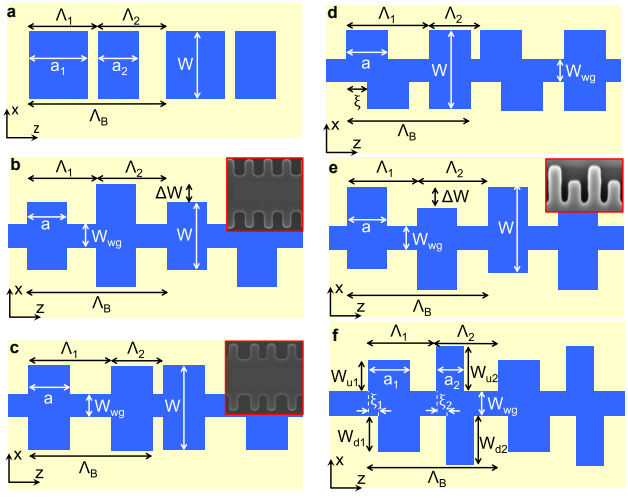

Figure 14: SWG-based Bragg filter geometries. The Bragg period Λ_B is divided in two slightly different subwavelength subperiods: Λ_1 and $\Lambda_2 = \Lambda_B - \Lambda_1$.
(a) Bragg filter assisted by a SWG with different duty cycles ($\Lambda_1 = \Lambda_2$, $a_1 \neq a_2$) [105,106], (b) SWG-based double-width-corrugation Bragg filter, DWCBF ($\Lambda_1 = \Lambda_2$, $\Delta W \neq 0$) [107], (c) Symmetric-corrugation shifted Bragg filter geometry, CSBF ($\Lambda_1 \neq \Lambda_2$) [108], (d) Asymmetric-corrugation shifted Bragg filter geometry, ACSBF ($\Lambda_1 \neq \Lambda_2$, $\xi \neq 0$) [108], (e) Multimode Bragg grating filter ($\Lambda_1 = \Lambda_2$, $\Delta W \neq 0$) [110], (f) Schematic representation indicating different parameters/degrees of freedom. Previous configurations (a–e) are particular realizations of this general case.

filters (DWCBF) with a length of 1 mm, high rejection ratio exceeding 40 dB, and bandwidths of 1.1 nm were experimentally demonstrated, using the differential corrugation widths of $\Delta W \sim 5$ nm.

Improved robustness against fabrication errors and superior performance can be achieved by adding more degrees of freedom to the SWG subperiod perturbation, such as corrugation asymmetries and shifts. Oser et al. experimentally demonstrated that the combination of SWG waveguides with shifted asymmetric corrugations yields subnanometer bandwidths and large rejection ratios [108]. Specifically, the authors obtain $\Delta\lambda = 0.8$ nm with a rejection exceeding 40 dB for a symmetric-corrugation shifted Bragg filter (CSBF) [Figure 14(c)] and $\Delta\lambda = 0.6$ nm with a rejection level of 16 dB for an asymmetric-corrugation shifted Bragg filter (ACSBF) [Figure 14(d)], in both cases for a filter length of 1 mm.

Multimode Bragg gratings in which the fundamental mode is coupled to the backward first-order mode is yet another class of grating filters. Ultrahigh rejection levels (in excess of 80 dB) can be achieved by cascading several filter sections using single-mode S-bend waveguides. First-order-mode back-reflections are radiated in the S-bends without affecting the propagation of the forward fundamental mode, thereby enabling efficient noncoherent cascading of Bragg filters [109]. In Ref. [110], an SWG-based multimode Bragg grating filter with asymmetric half-period shifted corrugation as shown in Figure 14(e) was proposed. The asymmetry of the structure is designed to achieve an efficient coupling of the forward fundamental mode to the back-reflected first-order mode. By applying the noncoherent cascading concept, the authors have implemented a nine-section multistage filter with a measured rejection level of 60 dB and a bandwidth $\Delta\lambda < 2$ nm. A schematic representation including all degrees of freedom is shown in Figure 14(f). A high rejection (60 dB) third-order Bragg filter based on a Si membrane long-period diffraction-less grating core was proposed by Alonso–Ramos et al. [29]. In this work, authors design the grating core to suppress diffraction effects despite working with periods much larger than typically used in SWG structures.

A different approach to develop SWG-based Bragg filters with subnanometer spectral bandwidths was proposed by Ctyroky et al. [111]. The structure, illustrated in Figure 15(a), is composed of a conventional SWG metamaterial waveguide (period Λ_{SWG}) loaded with an array of lateral silicon segments (period $\Lambda_B = 2\Lambda_{SWG}$) at a distance g from the SWG core. By engineering the refractive index, the modal field is delocalized from the SWG core to increase the overlap with the lateral loading segments, while maintaining the minimum feature size of the filter compatible with deep-ultraviolet (UV) lithography. The perturbation depends on the position of the lateral loading segments. The coupling coefficient κ exponentially decreases with the gap g because of the evanescent nature of the mode profile in the lateral cladding. Additionally, the longitudinal shifting ξ reduces the coupling coefficient as $\kappa(\xi) = \kappa(0)\cos(\pi\xi/\Lambda_B)$ [114]. These two mechanisms provide an efficient control of the rejection band, enabling the design of SWG metamaterial-core Bragg filters with subnanometer spectral bandwidths and a minimum feature size of 100 nm [111]. Using this technique, Cheben et al. have reported measured 3-dB bandwidths as small as $\Delta\lambda_{3\,dB} \approx 150$ pm, for a filter length of 4.7 mm and TM polarization [28]. This configuration has been proposed to realize a high-sensitivity integrated sensor working at 1310-nm wavelength [115]. In Ref. [116], Sun et al. demonstrated a discretely tunable optical delay line that uses an SWG metamaterial core loaded by lateral segments with a periodic perturbation in the gap distance. The authors have recently shown a tilted SWG-waveguide Bragg grating with lateral loading segments [112]. By a judicious optimization of the tilting angle of the SWG blocks, a polarization-dependent tuning of the central wavelength is achieved.

Complex Bragg filters with arbitrary spectral responses can be developed using a conventional SWG core with apodized lateral loading segments, as shown in Figure 15(b). In this filter configuration, the gap of each period, g_i, is modulated to produce a specific coupling coefficient κ_i, which is previously calculated from the target response by applying the layer-peeling algorithm [117]. The Bragg

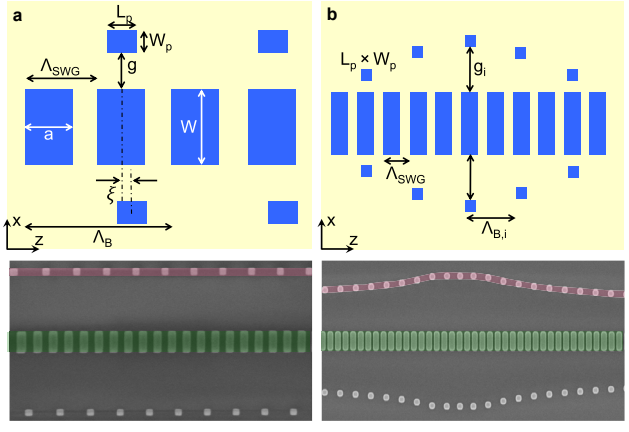

Figure 15: (a) Bragg filter with SWG metamaterial core and lateral silicon loading segments [28, 111], (b) Complex Bragg filter with arbitrary spectral response, composed of an SWG core with apodized lateral silicon loading segments [113].

period $\Lambda_{B,i}$ is slightly adjusted to synthesize the phase profile of the target impulse response, as well as to counteract the variations of the self coupling term caused by the lateral loading segments. Pereira-Martin et al. have validated this approach by designing an astrophotonic filter comprising 20 nonuniformly spaced narrow notches matching atmospheric OH radical emission lines near 1550-nm [113]. Two implementations of this filter were experimentally evaluated, using a homogeneous silicon waveguide core, which exhibits measured 3-dB linewidths within the range 220–470 pm for a filter length of 3.6 mm; and an SWG metamaterial waveguide core, with measured 3-dB linewidths of 210–340 pm for a filter length of 6.4 mm.

3.6 High-performance devices for wavelength and mode division multiplexing

To increase the aggregated data rate of optical links, various multiplexing schemes that enable the superposition of independent data channels in the same waveguide have been proposed. Recently, researchers have shown an increased interest in multiplexing techniques such as wavelength division multiplexing (WDM), mode division multiplexing (MDM), or PDM, among others [118]. In this section we will focus on WDM and MDM devices, as PDM devices were already reviewed in Section 3.4. A key building block for these techniques is the demultiplexer, a device that can spatially separate the different channels into different waveguides. In the last years, several researcher groups have reported WDM and MDM devices that benefit from SWG index and dispersion engineering to achieve a superior performance compared to conventional devices.

3.6.1 Wavelength-division multiplexing devices

SWG structures have been applied mainly to contradirectional couplers (contra DCs). Contra DCs comprise two asymmetric waveguides that are placed in proximity (see Figure 16). The forward propagating mode in one waveguide is phase matched to the backward propagating mode in the other waveguide through the −1 harmonic that is induced by a periodic perturbation. This is achieved for $n_1 + n_2 = \lambda_0/\Lambda$, where Λ is the perturbation period and $n_{1,2}$ are the effective indices of the two waveguides [119]. Unlike Bragg gratings, in which the reflected light is coupled back into the same waveguide, contra-DCs evade the need for circulators, which are difficult to implement on-chip in integrated photonics [120]. Moreover, contra-DCs exhibit low losses, virtually infinite free spectral range, and box-like channel passband, which are all characteristics advantageous for WDM systems. Conventional contra-DCs formed by strip waveguides suffer from weak coupling, which results in long devices and narrow bandwidth. SWG waveguides have been used in contra-DCs to engineer the coupling strength between the waveguides, in order to reduce the device footprint or tailor channel bandwidth [121–126]. In Refs. [121, 122], a strip waveguide is combined with an SWG waveguide to enhance the waveguide asymmetry while increasing the coupling strength, thus broadening the bandwidth, and reducing the device length. Another approach to attain the required asymmetry is to alternately offset the silicon blocks of both SWG waveguides [124]. In this work, the large mode delocalization of SWG waveguides resulted in an ultrawide channel bandwidth, as well as exceptionally low losses and low sidelobe suppression ratio (SLSR). Besides, contra-DCs allow for easy tuning, as their compact size provides efficient heating. This is shown in Ref. [126], where two independently controlled, thermally tuned contra-DCs are cascaded to develop an add-drop filter with tailorable bandwidth and central wavelength. In Ref. [125] the authors demonstrated that SWG-enabled contra-DCs are readily fabricable by deep-UV lithography. Table 3 summarizes the main performance metrics of recently reported contra-DCs. SWG engineering has also been applied, yet to a lesser extent, to other WDM devices. As shown in Ref. [127], SWG index engineering can be advantageously used to suppress most resonant modes of a ring-resonator-based demultiplexer, thus enlarging its free spectral range compared with conventional ring resonators. Except for

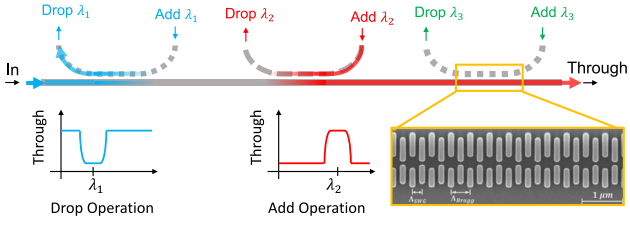

Figure 16: Schematic of a WDM demultiplexer based on a contra DC. Here we show three different contra DCs, each tuned at a different wavelength (λ_1, λ_2, and λ_3). The signal centerd around λ_1 enters the demultiplexers and is extracted by the first contra DC (blue signal path). The typical transmission spectrum from the input port to the through port of the first device is illustrated (Drop operation). The signal centerd around λ_2 is injected from the Add port of the second device into the bus waveguide. A schematic transmission response for this Add operation is also shown. The inset shows the SEM image of the contra DC reported in Ref. [124] (reproduced with permission from Ref. [124]).

Table 3: Performance comparison of recently demonstrated subwavelength-enhanced WDM (de)multiplexers based on contra DC.

Ref.	IL@λ_0 (dB)	3-dB BW (nm)	SLSR (dB)	ER (dB)	Notes
[121]	<1.8	6.7	<–20	<–20	
[122]	–	33.4	–2	–35	
[123]	<1	7–11	<–12	–	
[124]	0.26	32.6	<–19	<–40	
[125]	1.2	5	<–7	–30	O-band
[126]	2	6	–25	–	Tunable

SLSR, Side Lobe Suppression Ratio; IL, Insertion Loss; IB, Imbalance; BW, Bandwidth; ER, Extinction Ratio.

that work, the use of SWG metamaterials in ring-resonator configurations has been limited mainly to sensing applications (Section 3.8). Another device that benefits from SWG metamaterials for WDM applications is the asymmetric directional coupler (ADC). In Ref. [128], an ADC was utilized to develop a broadband demultiplexer for the O and L bands, achieving excellent performance (1 dB insertion loss and crosstalk lower than –15 dB) and a short device length compared to conventional non-SWG devices. Surface grating couplers as wavelength demultiplexers (e.g., [101]) will be reviewed in more detail in Section 3.7.

3.6.2 Mode-division multiplexing devices

MDM demultiplexers spatially separate the optical signals carried by different modes propagating in a multimode waveguide into various single-mode waveguides. Several MDM demultiplexing architectures have been explored, including asymmetric Y-junctions, asymmetric directional couplers (ADC) [129–131], contra-directional couplers [132], or adiabatic tapers [133] (see Figure 17). In the following we review how SWG metamaterials have been used to improve the multiplexing performance of some of these structures.

Adiabatic tapers are simple planar components with extremely broadband behavior that gradually transform an input mode into a target high-order mode [see Figure 16(a)]. These advantageous properties make them ideal building blocks for MDM demultiplexers. However, in order to ensure adiabaticity, conventional tapers need to be quite long (>100 µm) [134]. SWG metamaterials have been used to enhance the coupling strength and hence shorten the device length (~25 µm) [133].

An important drawback of adiabatic tapers is that they are limited to few-mode conversion. For many-mode demultiplexing, the preferred architecture is the asymmetric directional coupler, which can be readily cascaded in series along a bus waveguide to target different high-order modes. ADC-based mode demultiplexers are generally formed by a multi-mode waveguide and a single-mode waveguide that are placed parallelly and in proximity, as illustrated in Figure 17(b). The fundamental mode of the single-mode waveguide is phase matched to one of the high-order modes of the multi-mode waveguide. In this scenario, energy transfer between both waveguides is achieved provided the phase-matched modes have nonzero overlap integral [103]. However, when conventional waveguides are used, the phase-matching condition generally holds only for a narrow operational bandwidth and stringent fabrication tolerances. This is caused by the difference in the effective index change with the wavelength and geometry of both waveguides. This limitation has been successfully overcome by using SWG index and dispersion engineering in Ref. [129]. In this work, the SWG is designed to match the effective indices and their dependence on the waveguide width for both ADC arms at the same time. The authors experimentally demonstrated an 11-mode demultiplexer with crosstalk less than –15 dB and insertion loss less than 2.6 dB at the central wavelength. They also demonstrate that the fabricated device can tolerate waveguide width variations of ±20 nm.

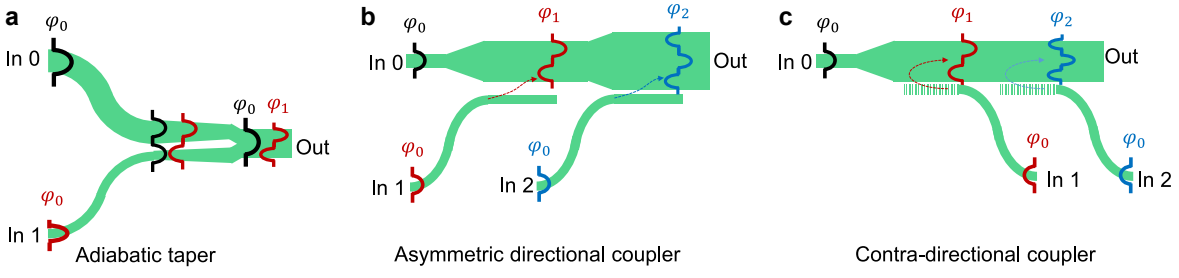

Figure 17: Schematics of typical mode multiplexing architectures that have benefited from SWG engineering: (a) Adiabatic taper, (b) asymmetric DC, and (c) contra DC. The input ports (In 0, 1, 2) support the fundamental mode (φ_0) that the demultiplexer converts to one of the high-order modes ($\varphi_{1,2}$).

Contra-directional couplers are not only relevant for wavelength division demultiplexing, but can also be used for mode division demultiplexing provided that the target modes are phase matched, as shown in Figure 17(c). In Ref. [132], the authors leverage SWG index engineering to develop contradirectional coupling between modes of different order and polarization, thereby attaining mode, wavelength, and polarization multiplexing functionalities in the same device.

It is also possible to achieve the mode-multiplexing functionality by an appropriate joint use of several fundamental building blocks. In Refs. [135, 136], the authors combine a broadband SWG MMI, a phase shifter, and a symmetric Y-junction to implement a compact two-mode demultiplexer that achieves a low measured insertion loss (0.55 dB) and a crosstalk less than –18 dB in an outstanding bandwidth of 120 nm in the C band. This broadband operation is a direct consequence of the ultra-wide bandwidth of the SWG MMI used compared with conventional MMI devices.

3.7 High-performance off-chip couplers

Off-chip couplers are the essential input/output interfaces in integrated photonics. They are primarily utilized for fiber-chip coupling, as planar silicon waveguides have sub-micrometric mode sizes that are much smaller than the mode field diameter of a standard (SMF-28) optical fiber [137]. Likewise, off-chip couplers have been recently used as optical nanoantennas for applications such as satellite optical communications and light detection and ranging (LiDAR), which require shaping and steering of the radiated beams [138]. Edge couplers and surface grating couplers are the most important off-chip coupling devices (see Figure 18). While the former are in-plane spot size converters at the chip facet, the latter enable vertical off-chip radiation and can be placed anywhere on the chip, thereby facilitating wafer-scale testing. A comprehensive review of the fundamental coupling strategies in silicon photonics circuits can be found in Ref. [139].

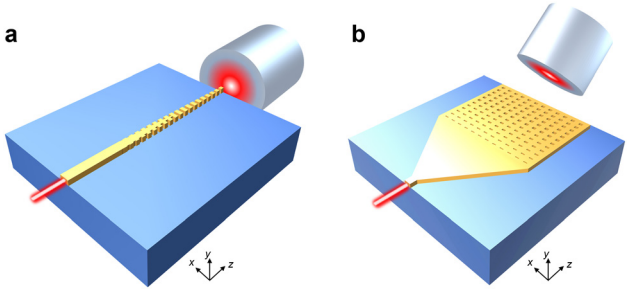

Figure 18: Schematics of SWG-based fiber-chip off-chip couplers. (a) Edge coupler with a subwavelength adiabatic transition. (b) Surface grating coupler with transverse subwavelength metamaterial patterning to apodize the radiated field profile.

3.7.1 Fiber-chip edge couplers

Subwavelength segmentation in edge couplers has been widely adopted since its early demonstration and subsequent refinement by Cheben et al. [8, 25, 140]. SWG metamaterial edge couplers comprise a subwavelength-patterned waveguide with a smooth decrease of the duty cycle and the core width to adiabatically adapt the guided Floquet–Bloch mode to the fundamental mode of the optical fiber at the chip facet [see Figure 18(a)]. Unlike conventional inverse tapers [141], the subwavelength metamaterial tapers enable local adjustment of the equivalent refractive index of the waveguide core by simply changing the grating duty cycle. This additional degree of freedom is exploited to achieve optimum matching between waveguide and fiber modes for both TE and TM polarization, resulting in a 90% coupling efficiency with negligible polarization dependent loss [25]. In Ref. [38], researchers at IBM and GLOBALFOUNDRIES optimized the SWG edge coupler concept for standard SMF-28 fibers by partially removing the silicon substrate to prevent leakage loss of the delocalized mode [142]. These couplers were fabricated in monolithic silicon photonics production lines and provide complete fiber self-alignment via precisely etched V-grooves, with better tolerances than solid-core inverse-taper couplers. Coupling efficiencies of –0.7 dB and –1.4 dB were reported for TE and TM polarizations, respectively, over a 1-dB bandwidth broader than 60 nm in the O band. Similar structures achieve back-reflections lower than –30 dB [39]. An alternative way to increase the misalignment tolerance of conventional solid-core edge couplers is the use of trident-shaped topologies [143]. Teng et al. enhanced the trident concept by SWG structuring to achieve polarization independency, with coupling losses ranging from 0.5 to 2 dB over C band [144]. A dual-trident SWG edge coupler has been demonstrated at 1550-nm wavelength and TE polarization, exhibiting a coupling loss lower than 2 dB in a bandwidth of 92 nm [145].

3.7.2 Fiber-chip surface grating couplers

First proposed by Halir et al. [13], transverse SWG structuring of surface grating couplers, illustrated in Figure 18(b), has become a customary strategy for radiation-strength apodization. Since then, SWG metamaterials have been used not only to improve the coupling efficiency of surface grating

couplers, but also to enlarge the bandwidth [146], to provide relaxed alignment tolerances [147], polarization insensitivity [148], and wavelength multiplexing for WDM applications [149], among others. The importance of SWG structuring of surface grating couplers is reflected in the number of articles that have been recently published to propose novel and efficient design techniques, including neural networks [150], machine learning [151], and weak form calculation and transformation optics [152].

Benedikovic et al. [71] leveraged subwavelength-grating properties to control both the upward diffraction efficiency and the field profile, thereby optimizing the directionality and the overlap with the fiber mode, achieving a theoretical coupling efficiency of up to 95%. Kamandar Dezfouli et al. used the degree of freedom introduced by subwavelength metamaterials to make the feature size of a perfectly vertical 75%-efficient grating coupler compatible with deep-UV lithography [153]. With the same aim, SWG structures were used in a bidirectional grating coupler with perfectly vertical radiation, achieving a respectable coupling efficiency (72% theoretically, 66% experimentally) for a minimum feature size larger than 100 nm [154]. Polarization insensitivity has been demonstrated by overlapping two perfectly vertical bidirectional grating couplers, arranged orthogonally. The resulting two-dimensional grating can also be SWG-apodized to improve the coupling efficiency (64% theoretically, 56% experimentally) [155]. As in the near-infrared telecom band, SWG apodization has proven useful also at mid-infrared wavelengths, where relaxed fabrication tolerances favor the utilization of subwavelength structures [156].

It is possible to broaden the bandwidth of surface grating couplers by reducing the group index of the grating [146]. This concept was exploited in Ref. [100] by leveraging SWG index engineering, obtaining simulated 3-dB bandwidths of 105 and 121 nm for TE and TM polarizations, respectively, yet at the expense of relatively low coupling efficiency. In Ref. [26] a different strategy to break the coupling efficiency–bandwidth trade-off was followed. The intrinsically narrowband nature of surface grating couplers was circumvented by using an SWG with zero-order radiation via a tilted silicon prism, yielding an unprecedented coupling efficiency–bandwidth product in excess of 75 nm (measured coupling efficiency of >80%, 1-dB bandwidth of 94 nm) [73].

The degrees of freedom introduced by SWGs can also facilitate the design of dual-band surface grating couplers, which handle light at two separate wavelengths, e.g. for WDM applications. In Ref. [149], the authors proposed a design strategy to tailor the separation of the coupling peaks and demonstrated dual-band focusing SWG grating couplers for a suspended 340-nm-thick SOI platform, with modest coupling efficiencies of 15–20% at central wavelengths in the range 1580–1660 nm. Following the same design flow and increasing the silicon thickness to 500 nm, the authors extended the operation to both near- and mid-infrared wavelengths simultaneously [157]. The device proposed in Ref. [101] couples the light from the optical fiber into two opposite output ports depending on the wavelength, thereby enabling demultiplexing at 1310 and 1550 nm. SWG sections are used to provide polarization independence with a minimum feature size of 100 nm, yielding coupling efficiencies around 35%. A similar approach has been recently shown to implement two-dimensional grating-coupling mode multiplexers for MDM [158].

3.7.3 Optical antennas

In the last few years, surface gratings couplers are being investigated as optical antennas. Embedded in optical phased arrays (OPAs), they are optimized to provide out-of-chip beam shaping and steering, which is required for LiDAR and free-space optical communications. In one-dimensional OPAs, the diffracted beam is steered in the two spatial directions using phase shifters (azimuthal direction) and wavelength scanning (elevation direction) [159]. Millimeter-long surface grating couplers can be utilized as optical antennas in 1D OPAs. By increasing the period of the loading segments, we have recently adapted the SWG-based Bragg-filter topology in Ref. [28] [see Figure 15(a)] to enable weak radiation [160], obtaining an experimental beam width of 0.1° and a wavelength sensitivity of 0.13°/nm, record metrics for deep-UV-compatible silicon-based optical antennas [161]. On the other hand, two-dimensional OPAs comprise a matrix of very short, densely packed antennas with strong radiation. In this case, phase shifters are used to steer the formed off-chip beam (in both azimuthal and elevation directions). An SWG-engineered deep-UV-compatible micro antenna concept with an impressive directionality of 94% and a 1-dB bandwidth of 230 nm was proposed by Khajavi et al. [162].

3.8 Optimized sensing waveguides

Silicon photonics is consolidating as one of the most promising technologies for developing cost-effective and portable lab-on-chip systems. Silicon-based waveguide sensors can detect the presence and concentration of biological and chemical species deposited onto the surface of the chip with high sensitivity and selectivity, which places

silicon photonics in an advantageous position compared with alternative platforms. This opens a wide spectrum of applications, ranging from point-of-care clinical diagnosis to environmental monitoring of greenhouse gases to food safety control, to name a few [163]

The operation principle of most photonic integrated sensors relies on the interaction between the evanescent tail of a guided mode and the target analyte, which is typically in the upper cladding of the waveguide to facilitate the flow of dissolutions. The sensing waveguides are embedded in sensing architectures to transform any change in the concentration of the analyte into a change in the effective index of the mode and then into a quantity that can be easily measured. For example, effective index variations are converted to power variations in interferometric architectures – e.g., Mach–Zehnder interferometers (MZIs) – and to resonance wavelength shifts in resonant architectures – e.g., ring resonators and photonic crystal (PhC) cavities [164]. Depending on the required specificity, two types of sensing approaches are possible: Surface and bulk. The former requires prior functionalization of the top and sidewalls surfaces of the waveguide with selective bioreceptors, to which the target molecules are bonded producing an increase of the thickness of the adsorbed layer ($S_{\mathrm{d,surf}} = \partial\lambda_{\mathrm{resonance}}/\partial t_{\mathrm{adsorbed\ layer}}$). On the other hand, bulk sensors detect changes in the cladding (analyte) refractive index ($S_{\mathrm{d,b}} = \partial\lambda_{\mathrm{resonance}}/\partial n_{\mathrm{cladding}}$).

SWG waveguides have proven to be convenient for sensing, because of their capability to increase the light-matter interaction [165–167]. Not only does the subwavelength segmentation delocalize the mode and thus increase the interaction volume, but it also creates a high field intensity between the silicon blocks, where the analyte is located. Using TE polarization, bulk waveguide sensitivities ($S_{\mathrm{w,b}} = \partial n_{\mathrm{eff}}/\partial n_{\mathrm{cladding}}$) of up to 0.8 (six-fold improvement compared with solid Si-core waveguide) and bulk device sensitivity ($S_{\mathrm{d,b}}$) above 400 nm/RIU have been achieved [165, 167, 168].

Over the past few years, research in SWG-based photonic integrated sensors has mainly been focused on four research directions. The first is the optimization of the waveguide dimensions. They should be carefully optimized to maximize sensitivity, while maintaining negligible leakage loss to substrate and feasible feature sizes. In Ref. [168], the bulk and surface sensitivities of SWG waveguides were calculated for a wide range of geometrical parameters (thicknesses, widths, and duty cycles), showing that silicon blocks that are narrower and thicker than those typically used in telecom applications (i.e., $W = 450$ nm, $H = 220$ nm) can provide bulk waveguide sensitivities close to unity. These results were confirmed by Milvich et al. by studying the surface sensitivity of various waveguide structures, including slot, double-slot, and conventional solid core waveguides, as well as different integration platforms (silicon nitride and SOI) and polarizations (TE and TM) [169]. Furthermore, in Ref. [170], the authors introduce a new parameter, the interaction efficiency, to quantify the probability of overlap between randomly distributed analyte molecules and the cladding mode field for different subwavelength waveguide geometries, thereby providing insight into the types of waveguides that yield more consistent and reliable sensing at low analyte concentrations. In Ref. [171], the authors thoroughly evaluate the trade-off between the mode confinement and the roughness-induced scattering loss of the most used sensing waveguides, including SWG waveguides.

The second important research direction includes investigation of new variants of SWG waveguides to further enhance sensing capabilities. The variants can be grouped in two different categories: (i) Multibox or multislot SWG waveguides and (ii) substrate over-etched SWG waveguides. The former combines the slot waveguide and the SWG waveguide by patterning the silicon segments in both the transverse and longitudinal directions [Figure 19(a) and (b)]. In addition to introducing more parameters to control the mode delocalization, this geometry provides an enlarged binding surface around each silicon block and an increased field intensity for the TE mode in the gaps [see the inset of Figure 19(b)], which significantly enhances the surface sensitivity. Experimental results were obtained in Ref. [172] for one slot [Figure 19(a)] and in Ref. [173] for four slots [Figure 19(b)], showing a two-fold enhancement in the surface sensitivity compared to the nominal SWG waveguide (2000 pm/nm vs 1000 pm/nm). The drawback of multi-box waveguides is that scattering losses are higher than in conventional strip and SWG waveguides, so that the improvement in sensitivity does not translate into an improvement in the intrinsic limit of detection, iLoD = $\lambda_o/Q \cdot S_d$, a figure of merit defined in Ref. [174]. On the other hand, in substrate over-etched SWG waveguides, the light–matter interaction can be enhanced by partially removing the buried oxide underneath to reduce the vertical asymmetry. Depending on the isotropy of the wet etching, two different types of waveguides have been obtained: The pedestal-SWG [175], shown in Figure 19(c), and the substrate over-etched-SWG [176], shown in Figure 19(d). In both cases, $S_{\mathrm{w,b}}$~1, and $S_{\mathrm{d,b}}$ of 545 nm/RIU and 575 nm/RIU are achieved, respectively, when the waveguides are embedded in a ring resonator architecture. The main drawback of the pedestal-SWG design is that,

in order to guarantee the mechanical stability, the maximum over-etching depth [V in Figure 19(c)] is limited by the length of the silicon blocks [I in Figure 19(c)].

The third line of research direction investigates new sensing architectures. Since the demonstration of the multibox SWG waveguide as a sensor [173], several works have tried to evaluate its performance in architectures other than ring resonators. For example, in Ref. [177], the multibox SWG waveguide is used in a phase-shifted Bragg grating (PSBG) resonator [Figure 19(e)]. Although the device sensitivity is almost the same as that of ring resonators, the absence of bends produces a smaller footprint (~200 versus 3000 μm^2) and a higher Q-factor (8000 versus 2600), which results in an improved iLoD (see Table 4). A similar performance was obtained in a photonic-crystal-based multibox SWG sensor in which a Bragg grating cavity is defined by gradually increasing the length of the silicon blocks from the center to the ends of the structure, as shown in Figure 19(f) [178]. In Ref. [179], the multislot SWG waveguide is designed to operate in the Bragg regime and, by using the first side lobe of the transmission spectrum as a sensing wavelength peak, a compact sensor with a length of only 9.5 µm and a sensitivity of 730 nm/RIU is experimentally demonstrated in a 340-nm-thick SOI platform [Figure 19(g)]. In relation to SWG-based interferometric architectures, some of the best performance has been achieved in Ref. [180]. Here, the concept of bimodal waveguide biosensor proposed in Ref. [181] is extended also to SWG waveguides, with promising experimental results ($S_{d,b}$ = 2270 nm/RIU) [see Figure 19(h)]. One-dimensional photonic crystal nanobeam cavities are also nano-periodic structures with an excellent potential for optical sensing applications – we refer the reader to a recent review paper on this topic [182].

The fourth line of action focuses on reducing the waveguide propagation loss, which can largely improve the limit of detection [183]. Since most of the analytes of interest are dissolved in aqueous solutions and the optical absorption of water is the main limiting loss factor in the sensor system at 1550-nm wavelength (α_{H_2O} = 52.5 dB/cm),

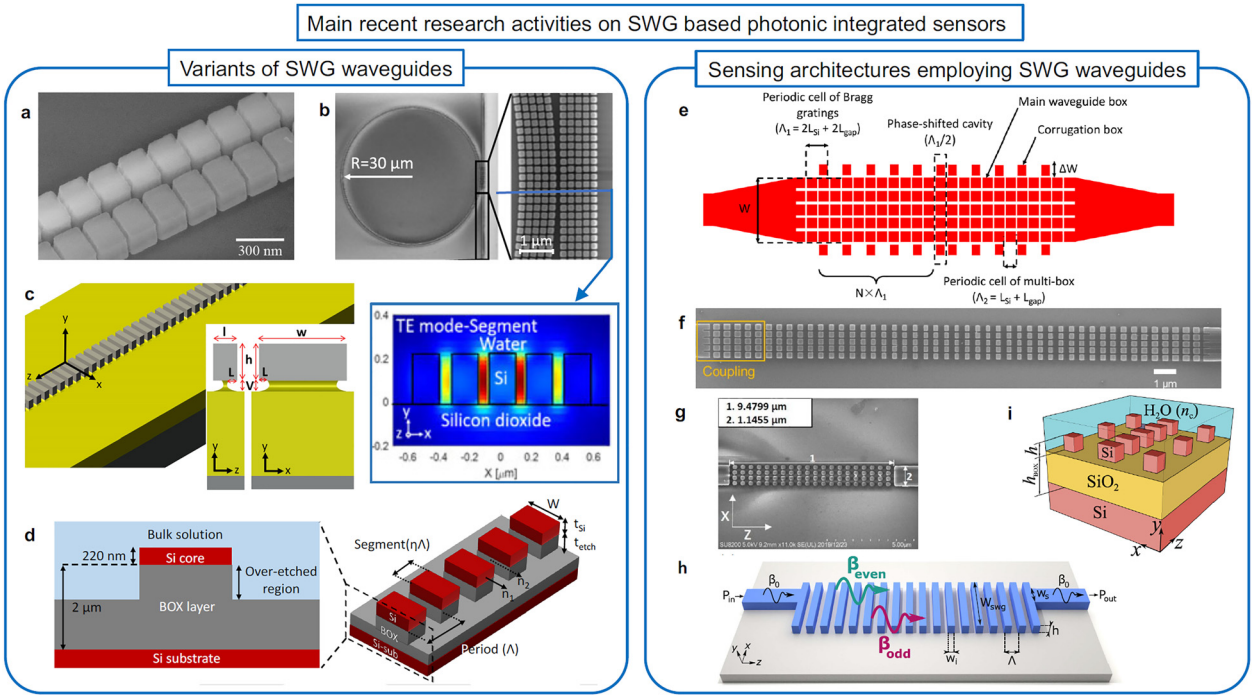

Figure 19: Summary of the most relevant recent works in SWG-based photonic integrated sensors.
(a) SEM image of the slot SWG waveguide (reproduced with permission from Ref. [172]). (b) SEM image of the multibox SWG waveguide embedded in a ring-resonator architecture. The inset shows the transverse electric field profile at the middle of the silicon blocks (reproduced with permission from Ref. [173]). (c) Schematic of the pedestal SWG waveguide (reproduced with permission from Ref. [175]). (d) Schematic of the SWG waveguide with over-etched substrate (reproduced with permission from Ref. [176]). (e) Schematic of the multibox SWG phase-shifted Bragg grating resonator, in which the external Si blocks of period Λ_2 constitute the Bragg corrugation (reproduced with permission from Ref. [177]). (f) SEM image of the multislot photonic crystal cavity (reproduced with permission from Ref. [178]). (g) SEM image of the multislot SWG Bragg grating (reproduced with permission from Ref. [179]). (h) Schematic of the bimodal SWG interferometric sensor (reproduced with permission from Ref. [180]). (i) Schematic of the SWG-based Bragg filter topology used as a sensor (reproduced with permission from Ref. [115]).

Table 4: Main performance metrics of SWG-based sensors.

Ref.	Waveguide/Architecture	$S_{w,b}$ (RIU/RIU)	$S_{d,b}$ (nm/RIU)	FSR (nm)	$iLoD_b$ ($\times 10^{-5}$ RIU)
[172]	Slot SWG/MZI	0.79	−599	13	n/a
[173]	Multislot SWG/Ring resonator	0.80	580	6	100
[175]	Pedestal SWG/Ring resonator	1.03	545	13	157
[176]	Substrate over-etched SWG/Ring resonator	0.97	575	5	175
[177]	Multislot SWG/Phase shifted Bragg grating	n/a	579	20	36
[178]	Multislot SWG/PhC cavity	–	586	>70	70
[179]	Multislot SWG/Bragg side lobe	n/a	730	n/a	n/a
[180]	Bimodal SWG/MZI	n/a	2270	~55	n/a
[115]	SWG/Narrowband Bragg filter	0.93	507	FSR free	5.1

increasing the waveguide sensitivity also increases the losses in the same proportion. This is the reason why all the aforementioned works did not significantly reduce the iLoD. Therefore, moving towards optical wavelengths with lower losses due to water absorption, like telecom O-band (λ_0 ~1310 nm; α_{H_2O} = 6.6 dB/cm), is a promising alternative. Some initial theoretical investigations have been made in this direction [115]. We explored a sensing architecture based on an SWG waveguide that is evanescently coupled to periodic lateral loading segments [Figure 19(i)], a novel SWG-based topology that was initially proposed for ultra-narrow Bragg filters (see Section 3.5, Ref. [111]). The simulation results showed a bulk sensitivity of 507 nm/RIU, a Q-factor of 4.9×10^4 and a iLoD of 5.1×10^{-5} RIU, the latter yielding about one order of magnitude improvement compared to state-of-the-art SWG-based sensors. Table 4 summarizes the main performance metrics of the discussed works. We believe that SWG waveguides for silicon photonics integrated sensors can pave the way for the development of future lab-on-chip applications.

3.9 Suspended waveguides for mid-infrared sensing and communications

The mid-infrared band is especially attractive for sensing applications, because the chemical bonds of the molecules of many organic and inorganic compounds resonantly absorb photons in this wavelength range (λ = 2–20 μm). From Soref's seminal paper [184], the interest in silicon photonics as a potential technology for integrated mid-infrared applications has steadily grown [185–187].

The standard SOI platform is not optimal for wavelengths above 4 μm, because of the prohibitive loss of the silicon dioxide layer [21]. Alternative materials have been proposed to cope with this inconvenience, including sapphire [188] and silicon nitride [189], but the operating range remains limited by the intrinsic losses of the lower cladding materials.

In suspended silicon membranes, the buried oxide (BOX) layer of the SOI wafer is removed by an acid solution delivered through a set of holes that are previously etched in the silicon layer [190, 191]. Suspended silicon membranes benefit from the entire transparency window of silicon, up to ~8 μm. As shown in Figure 20(a), SWGs are often utilized to define a lateral cladding with a three-fold function: (i) mechanically support the waveguide core, (ii) allow the flow of the hydrofluoric (HF) acid to etch the BOX layer, and (iii) synthesize a cladding-core index contrast required for waveguiding [see Figure 20(b)]. The latter produces lateral confinement within the waveguide core by only using a single reactive-ion etch step, which is an obvious advantage compared to membranes that require two steps to define a rib [190]. The design of SWG-cladding suspended waveguides requires a judicious selection of dimensional parameters to find a sweet spot for different requirements including mechanical robustness, fabrication feasibility, and low-loss single-mode optical guiding. A comprehensive analysis of SWG suspended waveguides can be found in Ref. [191].

Soler et al. reported a suspended silicon waveguide with lateral SWG cladding, at a wavelength of 3.8 μm [192]. Using a silicon thickness of 500 nm and a waveguide core width of 1.3 μm, a propagation loss as low as 0.82 dB/cm was achieved [193]. Other components such as MMI couplers and Mach–Zehnder interferometers were also implemented [193]. The first uncooled silicon waveguide-based bolometer was demonstrated for this suspended waveguide, with its surface being assisted by gold plasmonic antennas to absorb light and by amorphous silicon thermometers, yielding sensitivities up to 1.13 ± 0.04% change in resistance per milliwatt of input power [194].

The SWG suspended silicon waveguide concept was extended to λ_0 = 7.7 μm, the longest wavelength at which a

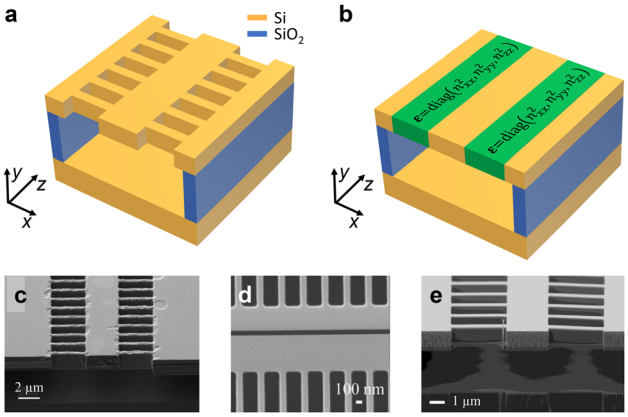

Figure 20: Schematics of (a) a suspended silicon waveguide with SWG lateral cladding and (b) its homogeneous model. SEM images of (c) the suspended silicon waveguide at 7.7-μm wavelength (reproduced with permission from Ref. [195]), (d) the suspended silicon slot waveguide at 2.2-μm wavelength (reproduced with permission from Ref. [197]), and (e) the suspended germanium waveguide at 7.7-μm wavelength.

silicon-based platform has yet been demonstrated. The silicon thickness was increased to 1.5 μm to minimize leakage losses toward the substrate. Similarly, a wider core of 2.9 μm was chosen to support the fundamental mode with low lateral leakage. An SEM image of this waveguide is shown in Figure 20(c). 90°- and S-bends with negligible losses were also reported [195].

In Ref. [196], the SWG-cladding suspended silicon platform was optimized for sensing at λ_0 = 2 μm. A commercial 340-nm-thick silicon layer was utilized for a trade-off between propagation losses and enhanced sensitivity to refractive index variations in the cladding. A quality factor Q of 15,300 was measured for a microracetrack resonator, for which a sensitivity of 337.5 nm/RIU was predicted. Zhou et al. developed a slot-waveguide suspended platform based on the same SWG-cladding geometry [197]. An SEM image of this structure is provided in Figure 20(d). Waveguides, curves, and racetrack resonators were demonstrated, yielding a propagation loss of 2.8 dB/cm, a bend loss of 0.15 dB per 90-degree curve, and an intrinsic optical Q factor of 12,600, respectively. These structures can potentially provide high sensitivity for applications up to a wavelength of 8 μm because of the high field concentration within the slot, enhancing the light interaction with the analyte.

At still longer wavelengths, $\lambda_0 > 8$ μm, the high absorption loss of silicon makes this material unsuitable for the guiding layer and germanium can be used instead. Recently, SWG-cladding suspended germanium waveguides with ~5 dB/cm propagation loss have been confirmed at 7.7 μm as a proof of concept, for TE polarization [198] [see Figure 20(e)]. For this platform, a suspended germanium micro-antenna was proposed as an input/output coupler between the chip and a long-wave chalcogenide optical fiber, with a design coupling efficiency of ~40%, a 1-dB bandwidth larger than 430 nm, and an angular bandwidth of ±10° [199]. This platform can potentially cover the entire transparency window of germanium, up to a wavelength of ~15 μm.

While initially targeted for the mid-infrared band, SWG-cladding suspended waveguides can be advantageously used for other wavelength ranges and applications as well as in novel waveguide platforms. A silicon-carbide-based platform was theoretically proposed for nonlinear applications and quantum photonics [200]. Since the base wafer comprises a thin layer of silicon carbide (n_{SiC} ~ 2.6) on silicon (n_{Si} ~ 3.5), here the suspension provides the vertical confinement for light guiding, while the SWG lateral cladding makes the silicon substrate accessible in a single dry etch step.

4 A "hands-on" with advanced subwavelength structures

In Section 2 we discussed the modeling of SWG structures using anisotropic metamaterials and showed that these models can provide accurate results, comparable to rigorous simulations of SWG waveguides in terms of modal analysis (see Figure 4). Here we aim to illustrate how these models can be leveraged to simplify the design and simulation of complex subwavelength-based devices. Specifically, we focus on the design of a polarization beam splitter and a waveguide lens, simulate them using the homogenization tools described in Section 2, and compare the results with rigorous, but time-consuming, 3D-FDTD simulation of the device with subwavelength geometry.

4.1 Broadband polarization beam splitter

As a first example of advanced devices based on subwavelength structures, we consider the broadband polarization beam splitter reported in Ref. [31]. The geometry of the device is shown in Figure 21(a) and consists of two parallel waveguides composed of a longitudinal subwavelength structure, with a transverse subwavelength structure between them. The basic idea is that for TM polarization (along the y direction) the electric field is parallel to the interfaces in both the longitudinal and the transverse subwavelength structures. Thus, for TM polarization the device "looks" homogeneous and acts as an MMI coupler

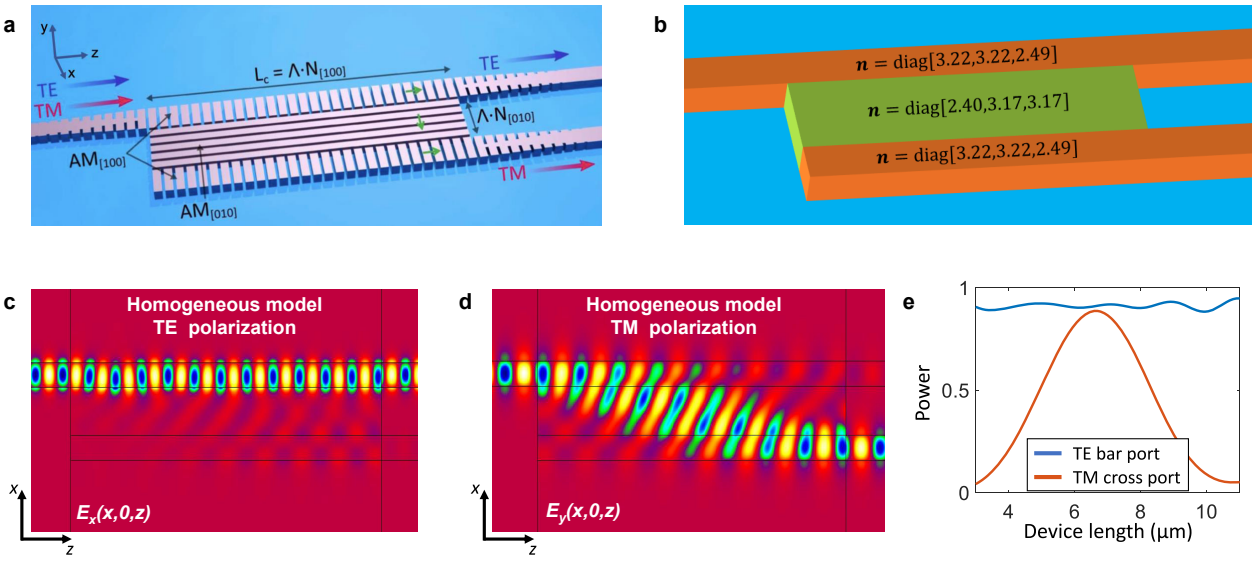

Figure 21: (a) A polarization splitter based on a dual subwavelength structure (reproduced with permission from Ref. [31]). (b) Using the anisotropic material models developed in Section 2, a much simpler, equivalent device can be constructed. (c, d) Electric field propagation obtained via modal simulation for TE and TM polarization through the equivalent device. (e) Power in the fundamental modes of the cross and bar ports as function of device length.

that forms an image of the input field at the cross port. For TE polarization (in the x–z plane) the transverse subwavelength structure suppresses coupling between the parallel waveguides [33], so that light from the input propagates to the bar port. While full simulation of this structure requires time-consuming 3D-FDTD techniques, in the following we show how, using the metamaterial models discussed in Section 2, simple modal simulations can be used to analyze this device.

The design is based on a subwavelength structure with a pitch of Λ = 250 nm. As discussed in Section 2, for this pitch the laminar model is usable, but the slab model yields very good results [see Figure 4]. We thus follow the steps outlined in Section 2.2 to obtain the equivalent metamaterial of the 250-nm-thick silicon layer, with a pitch of Λ = 250 nm, and a duty cycle of 74% and 70% for the longitudinal and transverse subwavelength structures, respectively. As a result, we obtain the diagonal index tensors for the equivalent structure shown in Figure 21(b). Note that the tensor for the transverse structure has been rotated by 90° using Eqs. (12) and (13), to account for the rotation in the coordinate system compared to Figures 3 and 4. From the refractive index tensors it is observed that indeed for TM polarization the device is virtually homogeneous, since the n_{yy} component is very similar in all the device. On the other hand, for TE polarization, the large n_{zz} component in the intermediate region enhances the field confinement inside that region [33]. The structure shown in Figure 21(b) can be readily analyzed with a mode propagation software [45], with significantly less computational effort than FDTD. The propagation of the electric field through the device for TE and TM polarization is shown in Figures 21(c) and 20(d), respectively. Notably, this comparatively simple model accurately predicts not only the polarization splitting behavior of the device, but also the optimal length: From Figure 21(e), obtained with the homogeneous model, the optimal device length is estimated in about 7.2 μm, which translates to 29 longitudinal periods, while the optimized value obtained in Ref. [31] via 3D-FDTD simulations of the subwavelength geometry is 30 periods.

4.2 Ultracompact GRIN-lens-based spot size converter

GRIN materials have demonstrated multiple applications in integrated photonics, including beam shaping [32, 72], waveguide bending [50, 51], waveguide crossing [53], or cloaking [201]. Subwavelength grating structures allow the synthesis of on-chip GRIN metamaterials [32, 47, 72] without requiring complex fabrication techniques such as grayscale lithography [55]. In this section we describe the design algorithm to synthesize a parabolic GRIN metamaterial. Then, we use the metamaterial to design a lens-based spot size converter, proposed in Ref. [32] and schematically shown in Figure 22(a). This device consists of a longitudinal SWG waveguide with constant period and an optimized duty cycle in the transverse direction, DC(x) =

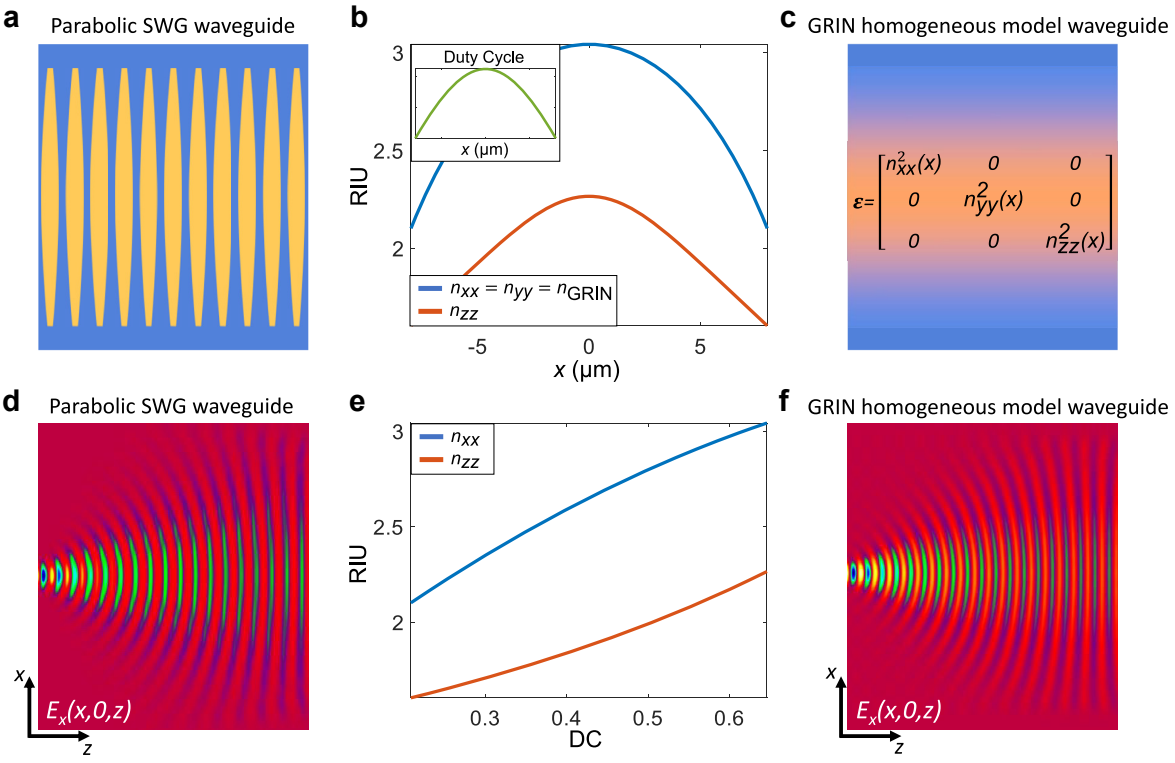

Figure 22: (a) Schematic representation of the SWG GRIN lens proposed in Ref. [32]. (b) Desired gradual index profile (n_{GRIN}) and the corresponding n_{zz} implemented with the proposed structure. Inset: Duty cycle apodization function DC(x) which implements the desired profile. (c) Schematic representation of the GRIN metamaterial which models the proposed structure. (d, f) Full-vectorial 3D-FDTD simulation of the electric field (R{$E_x(x,0,z)$}) propagating through a GRIN lens implemented with (d) a periodic SWG structure and (f) a gradual anisotropic metamaterial $\boldsymbol{\varepsilon}(x) = diag[n_{xx}^2(x), n_{yy}^2(x), n_{zz}^2(x)]$, with the indices shown in (b). (e) Metamaterial tensor components n_{xx} and n_{zz} as function the duty cycle DC = a/x.

$a(x)/\Lambda$. For illustration purposes we assume an operating wavelength $\lambda_0 = 1550$ nm, a silicon thickness $H = 220$ nm, a lens pitch $\Lambda = 240$ nm, and a lens width $w_{GRIN} = 16$ μm. The minimum gap at the center of the lens is set to 85 nm ($DC_{max} \sim 0.65$) to ensure fabrication feasibility. The design procedure to calculate the duty cycle function, DC(x), and the homogeneous anisotropic model of the GRIN core, $\boldsymbol{\varepsilon}(x) = \text{diag}[n_{xx}^2(x), n_{yy}^2(x), n_{zz}^2(x)]$, is summarized in Box 1.

Box 1: SWG metamaterial index design algorithm

① Calculate the tensor components of the homogeneous material model as a function of the duty cycle (Section 2):

$$\begin{cases} n_{xx}(\text{DC}) \\ n_{zz}(\text{DC}) \end{cases}$$

② Impose the GRIN goal function: $n_{xx}(x) = n_{GRIN}(x)$

③ Calculate the shape of the silicon segments using the mapping function calculated in ①:

$$n_{xx}(x) \overset{n_{xx}(\text{DC})}{\Rightarrow} \text{DC}(x)$$

④ Complete the anisotropic model by determining the remaining GRIN metamaterial tensor components:

$$\begin{cases} n_{yy}(x) = n_{xx}(x) \\ \text{DC}(x) \overset{n_{zz}(\text{DC})}{\Rightarrow} n_{zz}(x) \end{cases}$$

Step ①: We start from the homogenized material model described in Section 2, which allows the calculation of n_{xx}(DC) and n_{zz}(DC), i.e., the permittivity tensor components of the metamaterial as a function of the duty cycle. Step ②: We enforce that $n_{xx}(x)$ follow the desired GRIN function, which, in this specific case, is the parabolic law $n_{GRIN}(x) = n_0\sqrt{1-(\alpha x)^2}$, where n_0 is the refractive index at the center of the lens and α determines the curvature of the parabola [see Figure 22(b)]. Step ③: The shape of the silicon segments, DC(x), is calculated using n_{xx}(DC) as a lookup table. In this example, since n_{xx}(DC) is practically linear within the range DC ~ 0.25–0.65 [see Figure 22(e)], the duty cycle DC(x) is also a nearly parabolic function. Step ④: The remaining GRIN metamaterial tensor components are

determined, thereby completing the homogenization of the GRIN metamaterial.

To validate the proposed anisotropic model and the behavior of the SWG-based GRIN metamaterial, we compare the simulated field propagation through i) the periodic lens and ii) the homogeneous anisotropic lens defined by a gradual permittivity tensor $\boldsymbol{\varepsilon}(x) = \mathrm{diag}\,[n_{xx}^2(x), n_{yy}^2(x),\ n_{zz}^2(x)]$ [see Figure 22(c)]. We excite the modes of the structures with a $1 \times 0.22\ \mu m^2$ Gaussian beam. As shown in Figure 22(d) and (f), in both cases, the simulated structures operate as parabolic GRIN lenses, expanding and collimating the field profile distributions at specific distances: $f_{per} \sim 11\ \mu m$ and $f_{anis} \sim 12\ \mu m$. As expected, the homogeneous anisotropic model gives an accurate prediction of the device length ($f_{anis} \sim f_{per}$), which clearly confirms the appropriateness of the proposed homogenization technique. Even more, the SWG-based GRIN lens is significantly shorter than the homogeneous isotropic lens, which is mainly caused by the inherent anisotropy of the device (i.e., $n_{zz} \ll n_{xx}$).

5 Conclusions and outlook

Since the invention of silicon SWG metamaterial waveguides at the beginning of the millennium [8–16], research on these structures has been growing rapidly, with many impressive devices demonstrated for a wide range of applications. Indeed, the flexibility afforded by SWG metamaterial waveguides enables designers to choose the optimum material properties for each application. This has led to the demonstration of integrated photonic devices with unprecedented performance, often covering multiple or even all optical communications bands at the same time or extending the operation range of silicon photonic devices into mid-infrared. Significant advances have also been made in fiber-to-chip coupling, with solutions that offer sub-decibel coupling loss and ultra-broad bandwidths, both using edge and grating couplers. Indeed, as more research groups incorporate subwavelength structures into their design flows, the discovery of new SWG-engineered devices is expected to continue and expand into new application fields such as quantum photonics.

Subwavelength structures require feature sizes of the order of about 100 nm for operation in the near-infrared band. Such small features can be readily defined with e-beam lithography, but for conventional wafer-scale deep-UV lithography techniques, they are often at the limit of what can be reliably reproduced. To make the benefits of on-chip SWG metamaterials available to the wider silicon photonics industry, it is pivotal to overcome this technological limitation. Deep-UV immersion lithography with 60 nm resolution is being offered by several silicon photonics foundries, and some of them are already using SWG technology in their Process Design Kits [38, 202–204]. On the other hand, an effort is also being made to design geometries that enable subwavelength operation with larger feature sizes. A recent example is the bricked SWG waveguide [205], allowing substantially larger minimum feature sizes compared to conventional subwavelength structures. The bricked pattern only requires a single etch step and makes use of a Manhattan-like geometry, with a uniform grid and pixel dimensions as large as $150 \times 150\ nm^2$ for telecom wavelengths. We believe that the combination of advanced lithography techniques and novel subwavelength geometries will pave the way towards ever increasing adoption of subwavelength engineered devices in mass scale fabrication processes.

Notably, fabrication related constraints are relaxed significantly in the surging field of mid-infrared photonics, since the feature sizes scale directly with wavelength. Subwavelength structures are thus expected to play a key role in this field in the near future. In the visible wavelength range, silicon is opaque, and while silicon nitride offers low loss propagation, the main challenge for waveguide subwavelength structures again lies in reliable fabrication. For silicon nitride waveguides at a wavelength of 600 nm, the feature size for a subwavelength structure is of the order of 60 nm. Thus, in the visible wavelength range, subwavelength structures will become of increasing interest using high resolution deep-UV immersion lithography.

Of course, the use of subwavelength structures need not be limited to any specific material platform or wavelength range. When considering alternatives to existing approaches the focus should be on two questions. First, does the platform offer a high index contrast? Many of the advantages of subwavelength structure arise from the ability to tune the refractive index over a wide range, and given the nonresonant nature of subwavelength structures, this is only possible within the limits of the available index contrast. Second, is it possible to fabricate small enough feature sizes to achieve subwavelength operation? In this sense, CMOS-compatible materials such as silicon nitride and germanium will likely be explored, and more exotic materials such as diamond will also become of interest.

Author contributions: All the authors have accepted responsibility for the entire content of this submitted manuscript and approved submission.
Research funding: The authors acknowledge funding from Universidad de Málaga, Ministerio de Ciencia, Innovación y Universidades (MCIU) (PID2019-106747RB-I00), Ministerio

de Educación, Cultura y Deporte (MECD) (FPU16/06762, FPU16/03401); Consejería de Economía, Conocimiento, Empresas y Universidad (CECEU) (UMA18-FEDERJA-219, P18-RT-1453, P18-RT-793) and National Research Council of Canada (NRC) Collaborative Science, Technology and Innovation Program (CSTIP) (HTSN 209, HTSN 210).

Conflict of interest statement: The authors declare no conflicts of interest regarding this article.

References

[1] N. Yu and F. Capasso, "Flat optics with designer metasurfaces," *Nat. Mater.*, vol. 13, pp. 139–150, 2014.

[2] C. Della Giovampaola and N. Engheta, "Digital metamaterials," *Nat. Mater.*, vol. 13, pp. 1115–1121, 2014.

[3] Q. Wang, E. T. F. Rogers, B. Gholipour, et al., "Optically reconfigurable metasurfaces and photonic devices based on phase change materials," *Nat. Photonics*, vol. 10, pp. 60–65, 2016.

[4] S. Kruk and Y. Kivshar, "Functional meta-optics and nanophotonics governed by mie resonances," *ACS Photonics*, vol. 4, pp. 2638–2649, 2017.

[5] P. Lalanne and P. Chavel, "Metalenses at visible wavelengths: past, present, perspectives," *Laser Photon. Rev.*, vol. 11, p. 1600295, 2017.

[6] S. M. Kamali, E. Arbabi, A. Arbabi, and A. Faraon, "A review of dielectric optical metasurfaces for wavefront control," *Nanophotonics*, vol. 7, pp. 1041–1068, 2018.

[7] S. M. Rytov, "Electromagnetic properties of a finely stratified medium," *Sov. Phys. JETP*, vol. 2, pp. 466–475, 1956.

[8] P. Cheben, D.-X. Xu, S. Janz, and A. Densmore, "Subwavelength waveguide grating for mode conversion and light coupling in integrated optics," *Opt. Express*, vol. 14, pp. 4695–4702, 2006.

[9] P. Cheben, S. Janz, D.-X. Xu, B. Lamontagne, A. Delage, and S. Tanev, "A broad-band waveguide grating coupler with a subwavelength grating mirror," *IEEE Photonics Technol. Lett.*, vol. 18, pp. 13–15, 2006.

[10] J. H. Schmid, P. Cheben, S. Janz, J. Lapointe, E. Post, and D.-X. Xu, "Gradient-index antireflective subwavelength structures for planar waveguide facets," *Opt. Lett.*, vol. 32, pp. 1794–1796, 2007.

[11] J. H. Schmid, P. Cheben, S. Janz, et al., "Subwavelength grating structures in silicon-on-insulator waveguides," *Adv. Opt. Technol.*, vol. 18, pp. 16146–16155, 2008.

[12] P. J. Bock, P. Cheben, J. H. Schmid, et al., "Sub-wavelength grating mode transformers in silicon slab waveguides," *Opt. Express*, vol. 17, pp. 19120–19133, 2009.

[13] R. Halir, P. Cheben, S. Janz, D.-X. Xu, Í. Molina-Fernández, and J. G. Wangüemert-Pérez, "Waveguide grating coupler with subwavelength microstructures," *Opt. Lett.*, vol. 34, pp. 1408–1410, 2009.

[14] P. Cheben, S. Janz, D.-X. Xu, J. H. Schmid, A. Densmore, and J. Lapointe, *Interface Device for Performing Mode Transformation in Optical Waveguides*, 2010. U.S. patent US20080193080A1.

[15] J. H. Schmid, P. Cheben, P. J. Bock, et al., "Refractive index engineering with subwavelength gratings in silicon microphotonic waveguides," *IEEE Photonics J*, vol. 3, pp. 597–607, 2011.

[16] P. Cheben, P. J. Bock, J. H. Schmid, D.-X. Xu, A. Densmore, and S. Janz, *Composite subwavelength-structured Waveguide in Optical Systems*, 2013. U.S. patent US8503839B2.

[17] I. Staude and J. Schilling, "Metamaterial-inspired silicon nanophotonics," *Nat. Photonics*, vol. 11, pp. 274–284, 2017.

[18] P. Cheben, R. Halir, J. H. Schmid, H. A. Atwater, and D. R. Smith, "Subwavelength integrated photonics," *Nature*, vol. 560, pp. 565–572, 2018.

[19] A. H. Atabaki, S. Moazeni, F. Pavanello, et al., "Integrating photonics with silicon nanoelectronics for the next generation of systems on a chip," *Nature*, vol. 556, pp. 349–354, 2018.

[20] A. Bag, M. Neugebauer, U. Mick, S. Christiansen, S. A. Schulz, and P. Banzer, "Towards fully integrated photonic displacement sensors," *Nat. Commun.*, vol. 11, p. 2915, 2020.

[21] R. Soref, "Mid-infrared photonics in silicon and germanium," *Nat. Photonics*, vol. 4, pp. 495–497, 2010.

[22] J. Juan-Colás, A. Parkin, K. E. Dunn, M. G. Scullion, T. F. Krauss, and S. D. Johnson, "The electrophotonic silicon biosensor," *Nat. Commun.*, vol. 7, p. 12769, 2016.

[23] A. W. Elshaari, W. Pernice, K. Srinivasan, O. Benson, and V. Zwiller, "Hybrid integrated quantum photonic circuits," *Nat. Photonics*, vol. 14, pp. 285–298, 2020.

[24] K. Y. Yang, J. Skarda, M. Cotrufo, et al., "Inverse-designed non-reciprocal pulse router for chip-based LiDAR," *Nat. Photonics*, vol. 14, pp. 369–374, 2020.

[25] P. Cheben, J. H. Schmid, S. Wang, et al., "Broadband polarization independent nanophotonic coupler for silicon waveguides with ultra-high efficiency," *Opt. Express*, vol. 23, pp. 22553–22563, 2015.

[26] A. Sánchez-Postigo, J. Gonzalo Wangüemert-Pérez, J. M. Luque-González, et al., "Broadband fiber-chip zero-order surface grating coupler with 0.4 dB efficiency," *Opt. Lett.*, vol. 41, pp. 3013–3016, 2016.

[27] D. Benedikovic, C. Alonso-Ramos, D. Pérez-Galacho, et al., "L-shaped fiber-chip grating couplers with high directionality and low reflectivity fabricated with deep-UV lithography," *Opt. Lett.*, vol. 42, pp. 3439–3442, 2017.

[28] P. Cheben, J. Čtyroký, J. H. Schmid, et al., "Bragg filter bandwidth engineering in subwavelength grating metamaterial waveguides," *Opt. Lett.*, vol. 44, pp. 1043–1046, 2019.

[29] C. Alonso-Ramos, X. Le Roux, J. Zhang, et al., "Diffraction-less propagation beyond the sub-wavelength regime: a new type of nanophotonic waveguide," *Sci. Rep.*, vol. 9, p. 5347, 2019.

[30] R. Halir, P. Cheben, J. M. Luque-González, et al., "Ultra-broadband nanophotonic beamsplitter using an anisotropic sub-wavelength metamaterial," *Laser Photon. Rev.*, vol. 10, pp. 1039–1046, 2016.

[31] H. Xu, D. Dai, and Y. Shi, "Ultra-broadband and ultra-compact on-chip silicon polarization beam splitter by using hetero-anisotropic metamaterials," *Laser Photon. Rev.*, vol. 13, p. 1800349, 2019.

[32] J. M. Luque-González, R. Halir, J. G. Wangüemert-Pérez, et al., "An ultracompact GRIN-lens-based spot size converter using subwavelength grating metamaterials," *Laser Photon. Rev.*, vol. 13, p. 1900172, 2019.

[33] S. Jahani, S. Kim, J. Atkinson, et al., "Controlling evanescent waves using silicon photonic all-dielectric metamaterials for dense integration," *Nat. Commun.*, vol. 9, p. 1893, 2018.

[34] Q. Liu, S. Li, B. Wang, et al., "Efficient mode transfer on a compact silicon chip by encircling moving exceptional points," *Phys. Rev. Lett.*, vol. 124, p. 153903, 2020.
[35] T. Hu, C.-K. Tseng, Y. H. Fu, et al., "Demonstration of color display metasurfaces via immersion lithography on a 12-inch silicon wafer," *Opt. Express*, vol. 26, p. 19548, 2018.
[36] J. H. Song, T. D. Kongnyuy, B. Troia, et al., "Grating devices on a silicon nitride technology platform for visible light applications," *OSA Contin.*, vol. 2, pp. 1155–1165, 2019.
[37] R. Halir, L. Zavargo-Peche, D. X. Xu, et al., "Single etch grating couplers for mass fabrication with DUV lithography," *Opt. Quantum Electron.*, vol. 44, pp. 521–526, 2012.
[38] T. Barwicz, B. Peng, R. Leidy, et al., "Integrated metamaterial interfaces for self-aligned fiber-to-chip coupling in volume manufacturing," *IEEE J. Sel. Top. Quantum Electron.*, vol. 25, p. 4700313, 2019.
[39] B. Peng, T. Barwicz, Y. Bian, et al., "Controlling optical return loss in production silicon photonic metamaterial fiber couplers," *Opt. Lett.*, vol. 46, pp. 400–403, 2021.
[40] R. Halir, P. J. Bock, P. Cheben, et al., "Waveguide sub-wavelength structures : a review of principles," *Laser Photon. Rev.*, vol. 49, pp. 25–49, 2015.
[41] R. Halir, A. Ortega-Moñux, D. Benedikovic, et al., "Subwavelength-grating metamaterial structures for silicon photonic devices," *Proc. IEEE*, vol. 106, pp. 2144–2157, 2018.
[42] P. Yeh, A. Yariv, and C.-S. Hong, "Electromagnetic propagation in periodic stratified media I General theory*," *J. Opt. Soc. Am.*, vol. 67, pp. 423–438, 1977.
[43] B. E. A. Saleh and M. C. Teich, "Fundamentals of photonics," in *Wiley Series in Pure and Applied Optics*, New York, John Wiley & Sons, Inc, 1991.
[44] FULLWAVE FDTD Simulation Software," https://www.synopsys.com/optical-solutions/rsoft/passive-device-fullwave.html.
[45] Photon Design, "FIMMWAVE Photon Design mode solver," https://www.photond.com/products/fimmwave.htm.
[46] "BANDSOLVE Photonic band structure software," https://www.synopsys.com/photonic-solutions/rsoft-photonic-device-tools/passive-device-bandsolve.html.
[47] U. Levy, M. Abashin, K. Ikeda, A. Krishnamoorthy, J. Cunningham, and Y. Fainman, "Inhomogenous dielectric metamaterials with space-variant polarizability," *Phys. Rev. Lett.*, vol. 98, p. 243901, 2007.
[48] J. M. Luque-González, A. Herrero-Bermello, A. Ortega-Moñux, et al., "Tilted subwavelength gratings: controlling anisotropy in metamaterial nanophotonic waveguides," *Opt. Lett.*, vol. 43, pp. 4691–4694, 2018.
[49] Z. Wang, X. Xu, D. Fan, Y. Wang, and R. T. Chen, "High quality factor subwavelength grating waveguide micro-ring resonator based on trapezoidal silicon pillars," *Opt. Lett.*, vol. 41, pp. 3375–3378, 2016.
[50] H. Wu, C. Li, L. Song, H.-K. Tsang, J. E. Bowers, and D. Dai, "Ultra-sharp multimode waveguide bends with subwavelength gratings," *Laser Photon. Rev.*, vol. 13, p. 1800119, 2019.
[51] H. Xu and Y. Shi, "Ultra-sharp multi-mode waveguide bending assisted with metamaterial-based mode converters," *Laser Photon. Rev.*, vol. 12, p. 1700240, 2018.
[52] P. J. Bock, P. Cheben, J. H. Schmid, et al., "Subwavelength grating crossings for silicon wire waveguides," *Opt. Express*, vol. 18, pp. 16146–16155, 2010.
[53] Q. Wu, J. P. Turpin, and D. H. Werner, "Integrated photonic systems based on transformation optics enabled gradient index devices," *Light Sci. Appl.*, vol. 1, p. e38, 2012.
[54] S. H. Badri and M. M. Gilarlue, "Silicon nitride waveguide devices based on gradient-index lenses implemented by subwavelength silicon grating metamaterials," *Appl. Opt.*, vol. 59, pp. 5269–5275, 2020.
[55] L. H. Gabrielli, D. Liu, S. G. Johnson, and M. Lipson, "On-chip transformation optics for multimode waveguide bends," *Nat. Commun.*, vol. 3, pp. 1216–1217, 2012.
[56] C. Li, D. Liu, and D. Dai, "Multimode silicon photonics," *Nanophotonics*, vol. 8, pp. 227–247, 2018.
[57] W. Shi, Y. Tian, and A. Gervais, "Scaling capacity of fiber-optic transmission systems via silicon photonics," *Nanophotonics*, vol. 9, pp. 4629–4633, 2020.
[58] J. Xiao and Z. Guo, "Ultracompact polarization-insensitive power splitter using subwavelength gratings," *IEEE Photonics Technol. Lett.*, vol. 30, pp. 529–532, 2018.
[59] L. Lu, D. Liu, M. Yan, and M. Zhang, "Subwavelength adiabatic multimode Y-junctions," *Opt. Lett.*, vol. 44, pp. 4729–4732, 2019.
[60] D. González-Andrade, C. Lafforgue, E. Durán-Valdeiglesias, et al., "Polarization- and wavelength-agnostic nanophotonic beam splitter," *Sci. Rep.*, vol. 9, p. 3604, 2019.
[61] J. M. Fargas Cabanillas, B. Zhang, and M. A. Popović, "Demonstration of 3±0.12 dB power splitting over 145 nm optical bandwidth in a 31-µm long 3-dB rapid adiabatic coupler," in *Optical Fiber Communication Conference (OFC)*, San Diego, CA, USA, OSA, 2020, p. Th1A.2.
[62] H. Yun, L. Chrostowski, and N. A. F. Jaeger, "Ultra-broadband 2 × 2 adiabatic 3 dB coupler using subwavelength-grating-assisted silicon-on-insulator strip waveguides," *Opt. Lett.*, vol. 43, pp. 1935–1938, 2018.
[63] L. Xu, Y. Wang, A. Kumar, et al., "Compact high-performance adiabatic 3-dB coupler enabled by subwavelength grating slot in the silicon-on-insulator platform," *Opt. Express*, vol. 26, pp. 29873–29885, 2018.
[64] R. Halir, A. Maese-Novo, A. Ortega-Moñux, et al., "Colorless directional coupler with dispersion engineered sub-wavelength structure," *Opt. Express*, vol. 20, pp. 13470–13477, 2012.
[65] C. Ye and D. Dai, "Ultra-compact broadband 2 × 2 3 dB power splitter using a subwavelength-grating-assisted asymmetric directional coupler," *J. Light. Technol.*, vol. 38, pp. 2370–2375, 2020.
[66] A. Ortega-Moñux, C. Alonso-Ramos, A. Maese-Novo, et al., "An ultra-compact multimode interference coupler with a subwavelength grating slot," *Laser Photonics Rev.*, vol. 7, pp. 12–15, 2013.
[67] W. Zhong and J. Xiao, "Ultracompact polarization-insensitive power splitter using subwavelength-grating-based MMI couplers on an SOI platform," *Appl. Opt.*, vol. 59, pp. 1991–1997, 2020.
[68] D. González-Andrade, J. M. Luque-González, J. Gonzalo Wangüemert-Pérez, et al., "Ultra-broadband nanophotonic phase shifter based on subwavelength metamaterial waveguides," *Photonics Res.*, vol. 8, pp. 359–367, 2020.
[69] H. Xu, D. Dai, and Y. Shi, "Ultra-broadband on-chip multimode power splitter with an arbitrary splitting ratio," *OSA Contin.*, vol. 3, pp. 1212–1221, 2020.

[70] Y. Liu, Z. Li, S. Wang, et al, "Ultra-compact and polarization-insensitive MMI coupler based on inverse design," in *Optical Fiber Communication Conference (OFC)*, San Diego, CA, USA, OSA, 2019, p. W3B.7.
[71] D. Benedikovic, C. Alonso-Ramos, S. Guerber, et al., "Sub-decibel silicon grating couplers based on L-shaped waveguides and engineered subwavelength metamaterials," *Opt. Express*, vol. 27, pp. 26239–26250, 2019.
[72] Z. Zhang, Y. Tong, Y. Wang, and H. K. Tsang, "Nonparaxial mode-size converter using an ultracompact metamaterial Mikaelian lens," *J. Light. Technol.*, vol. 39, pp. 2077–2083, 2021.
[73] A. Sánchez-Postigo, R. Halir, J. G. Wangüemert-Pérez, et al., "Breaking the coupling efficiency–bandwidth trade-off in surface grating couplers using zero-order radiation," *Laser Photon. Rev.*, vol. 15, p. 2000542, 2021.
[74] S. Kim, D. A. Westly, B. J. Roxworthy, et al., "Photonic waveguide to free-space Gaussian beam extreme mode converter," *Light Sci. Appl.*, vol. 7, p. 72, 2018.
[75] N. V Sapra, K. Y. Yang, D. Vercruysse, et al., "On-chip integrated laser-driven particle accelerator," Science, vol. 83, pp. 79–83, 2020.
[76] P. J. Bock, P. Cheben, J. H. Schmid, et al., "Demonstration of a curved sidewall grating demultiplexer on silicon," *Opt. Express*, vol. 20, pp. 19882–19892, 2012.
[77] Y. Fu, T. Ye, W. Tang, and T. Chu, "Efficient adiabatic silicon-on-insulator waveguide taper," *Photonics Res.*, vol. 2, pp. A41–A44, 2014.
[78] W. Qi, Y. Yu, and X. Zhang, "On-chip arbitrary-mode spot size conversion," *Nanophotonics*, vol. 9, pp. 4365–4372, 2020.
[79] Z. Wang, T. Li, A. Soman, D. Mao, T. Kananen, and T. Gu, "On-chip wavefront shaping with dielectric metasurface," *Nat. Commun.*, vol. 10, p. 3547, 2019.
[80] A. Hadij-ElHouati, P. Cheben, A. Ortega-Moñux, et al., "Distributed Bragg deflector coupler for on-chip shaping of optical beams," *Opt. Express*, vol. 27, pp. 33180–33193, 2019.
[81] A. Hadij-ElHouati, P. Cheben, A. Ortega-Moñux, et al., "High-efficiency conversion from waveguide mode to an on-chip beam using a metamaterial engineered Bragg deflector," *Opt. Lett.*, vol. 46, pp. 2409–2412, 2021.
[82] T. Huang, Y. Xie, Y. Wu, Z. Cheng, S. Zeng, and P. S. Ping, "Compact polarization beam splitter assisted by subwavelength grating in triple-waveguide directional coupler," *Appl. Opt.*, vol. 58, pp. 2264–2268, 2019.
[83] F. Zhang, J. Zheng, Y. Song, W. Liu, P. Xu, and A. Majumdar, "Ultra-broadband and compact polarizing beam splitter in silicon photonics," *OSA Contin.*, vol. 3, pp. 560–567, 2020.
[84] J. M. Luque-González, A. Herrero-Bermello, A. Ortega-Moñux, et al., "Polarization splitting directional coupler using tilted subwavelength gratings," *Opt. Lett.*, vol. 45, pp. 3398–3401, 2020.
[85] J. Yang, Y. Dong, Y. Xu, B. Zhang, and Y. Ni, "Broadband and high-extinction-ratio polarization beam splitter on tilted subwavelength gratings waveguides," *Appl. Opt.*, vol. 59, pp. 7705–7711, 2020.
[86] C.-C. Huang and C.-C. Huang, "Ultra-compact and high-performance polarization beam splitter assisted by slotted waveguide subwavelength gratings," *Sci. Rep.*, vol. 10, p. 12841, 2020.
[87] K. Chen, K. Yu, and S. He, "High performance polarization beam splitter based on cascaded directional couplers assisted by effectively anisotropic structures," *IEEE Photonics J.*, vol. 11, pp. 1–9, 2019.
[88] L. Xu, Y. Wang, A. Kumar, et al., "Polarization beam splitter based on MMI coupler with SWG birefringence engineering on SOI," *IEEE Photonics Technol. Lett.*, vol. 30, pp. 403–406, 2018.
[89] A. Herrero-Bermello, J. M. Luque-González, A. V. Velasco, A. Ortega-Moñux, P. Cheben, and R. Halir, "Design of a broadband polarization splitter based on anisotropy-engineered tilted subwavelength gratings," *IEEE Photonics J.*, vol. 11, p. 6601508, 2019.
[90] A. Herrero-Bermello, A. Dias-Ponte, J. M. Luque-González, et al., "Experimental demonstration of metamaterial anisotropy engineering for broadband on-chip polarization beam splitting," *Opt. Express*, vol. 28, pp. 16385–16393, 2020.
[91] M. R. Watts, H. A. Haus, and E. P. Ippen, "Integrated mode-evolution-based polarization splitter," *Opt. Lett.*, vol. 30, pp. 967–969, 2005.
[92] C. Li, M. Zhang, J. E. Bowers, and D. Dai, "Ultra-broadband polarization beam splitter with silicon subwavelength-grating waveguides," *Opt. Lett.*, vol. 45, pp. 2259–2262, 2020.
[93] H. Xu and Y. Shi, "Subwavelength-grating-assisted silicon polarization rotator covering all optical communication bands," *Opt. Express*, vol. 27, pp. 5588–5597, 2019.
[94] M. Ma, A. H. K. Park, Y. Wang, et al., "Sub-wavelength grating-assisted polarization splitter-rotators for silicon-on-insulator platforms," *Opt. Express*, vol. 27, pp. 17581–17591, 2019.
[95] H. Xu, D. Dai, and Y. Shi, "Anisotropic metamaterial-assisted all-silicon polarizer with 415-nm bandwidth," *Photonics Res.*, vol. 7, pp. 1432–1439, 2019.
[96] B. Ni and J. Xiao, "Subwavelength-grating-based compact and broadband TE-pass polarizer for slot waveguides on a SOI platform," *J. Opt. Soc. Am. B*, vol. 36, pp. 2126–2133, 2019.
[97] H. Xie, J. Zheng, P. Xu, J. Yao, J. Whitehead, and A. Majumdar, "Ultra-compact subwavelength-grating-assisted polarization-independent directional coupler," *IEEE Photonics Technol. Lett.*, vol. 31, pp. 1538–1541, 2019.
[98] Y. Chen and J. Xiao, "Compact silicon-based polarization-independent directional coupler using subwavelength gratings," *Appl. Opt.*, vol. 58, pp. 7430–7435, 2019.
[99] N. Yang and J. Xiao, "A compact silicon-based polarization-independent power splitter using a three-guide directional coupler with subwavelength gratings," *Opt. Commun.*, vol. 459, p. 125095, 2020.
[100] N. Purwaha, A. Atieh, and W. N. Ye, "Broadband and polarization flexible SOI grating coupler based on sub-wavelength gratings with low back reflections," *OSA Contin.*, vol. 2, pp. 1350–1357, 2019.
[101] T. Hao, A. Sánchez-Postigo, P. Cheben, A. Ortega-Moñux, and W. N. Ye, "Dual-band polarization-independent subwavelength grating coupler for wavelength demultiplexing," *IEEE Photonics Technol. Lett.*, vol. 32, pp. 1163–1166, 2020.
[102] A. Herrero-Bermello, J. M. Luque-González, R. Halir, et al., "Zero-birefringence silicon waveguides based on tilted subwavelength metamaterials," *IEEE Photonics J.*, vol. 11, p. 2700308, 2019.
[103] C.-L. Chen, *Foundations for Guided-Wave Optics*, John Wiley & Sons, Inc., 2006.
[104] X. Wang, W. Shi, R. Vafaei, N. A. F. Jaeger, and L. Chrostowski, "Uniform and sampled Bragg gratings in SOI strip waveguides with sidewall corrugations," *IEEE Photonics Technol. Lett.*, vol. 23, pp. 290–292, 2011.

[105] J. Wang, I. Glesk, and L. R. Chen, "Subwavelength grating filtering devices," *Opt. Express*, vol. 22, pp. 15335–15345, 2014.
[106] J. Wang, I. Glesk, and L. R. Chen, "Subwavelength grating Bragg grating filters in silicon-on-insulator," *Electron. Lett.*, vol. 51, pp. 712–714, 2015.
[107] D. Pérez-Galacho, C. Alonso-Ramos, F. Mazeas, et al., "Optical pump-rejection filter based on silicon sub-wavelength engineered photonic structures," *Opt. Lett.*, vol. 42, pp. 1468–1471, 2017.
[108] D. Oser, D. Pérez-Galacho, C. Alonso-Ramos, et al., "Subwavelength engineering and asymmetry: two efficient tools for sub-nanometer-bandwidth silicon Bragg filters," *Opt. Lett.*, vol. 43, pp. 3208–3211, 2018.
[109] D. Oser, F. Mazeas, X. Le Roux, et al., "Coherency-broken Bragg filters: overcoming on-chip rejection limitations," *Laser Photon. Rev.*, vol. 13, p. 1800226, 2019.
[110] D. Oser, D. Pérez-Galacho, X. Le Roux, et al., "Silicon subwavelength modal Bragg grating filters with narrow bandwidth and high optical rejection," *Opt. Lett.*, vol. 45, pp. 5784–5787, 2020.
[111] J. Čtyroký, J. Gonzalo Wangüemert-Pérez, P. Kwiecien, et al., "Design of narrowband Bragg spectral filters in subwavelength grating metamaterial waveguides," *Opt. Express*, vol. 26, pp. 179–194, 2018.
[112] H. Sun and L. R. Chen, "Polarization-dependent tuning of Bragg reflection enabled through tilted subwavelength grating waveguide Bragg gratings," *Opt. Lett.*, vol. 46, pp. 1450–1453, 2021.
[113] D. Pereira-Martín, J. M. Luque-González, J. Gonzalo Wangüemert-Pérez, et al., "Complex spectral filters in silicon waveguides based on cladding-modulated Bragg gratings," *Opt. Express*, vol. 29, pp. 15867–15881, 2021.
[114] X. Wang, Y. Wang, J. Flueckiger, et al., "Precise control of the coupling coefficient through destructive interference in silicon waveguide Bragg gratings," *Opt. Lett.*, vol. 39, pp. 5519–5522, 2014.
[115] C. Pérez-Armenta, A. Ortega-Moñux, J. Čtyroký, et al., "Narrowband Bragg filters based on subwavelength grating waveguides for silicon photonic sensing," *Opt. Express*, vol. 28, pp. 37971–37985, 2020.
[116] H. Sun, Y. Wang, and L. R. Chen, "Integrated discretely tunable optical delay line based on step-chirped subwavelength grating waveguide Bragg gratings," *J. Light. Technol.*, vol. 38, pp. 5551–5560, 2020.
[117] J. Skaar, L. Wang, and T. Erdogan, "On the synthesis of fiber Bragg gratings by layer peeling," *IEEE J. Quantum Electron.*, vol. 37, pp. 165–173, 2001.
[118] D. Dai, "Silicon nanophotonic integrated devices for on-chip multiplexing and switching," *J. Light. Technol.*, vol. 35, pp. 572–587, 2017.
[119] P. Yeh and H. F. Taylor, "Contradirectional frequency-selective couplers for guided-wave optics," *Appl. Opt.*, vol. 19, pp. 2848–2855, 1980.
[120] W. Shi, X. Wang, C. Lin, et al., "Silicon photonic grating-assisted, contra-directional couplers," *Opt. Express*, vol. 21, pp. 3633–3650, 2013.
[121] B. Naghdi and L. R. Chen, "Silicon photonic four-channel optical add-drop multiplexer enabled by subwavelength grating waveguides," *IEEE Photonics J.*, vol. 10, pp. 1–10, 2018.
[122] D. Charron, J. St-Yves, O. Jafari, S. LaRochelle, and W. Shi, "Subwavelength-grating contradirectional couplers for large stopband filters," *Opt. Lett.*, vol. 43, pp. 895–898, 2018.
[123] J. Chen and Y. Shi, "Flat-top CWDM (de)multiplexers based on contra-directional couplers with subwavelength gratings," *IEEE Photonics Technol. Lett.*, vol. 31, pp. 2003–2006, 2019.
[124] H. Yun, M. Hammood, S. Lin, L. Chrostowski, and N. A. F. Jaeger, "Broadband flat-top SOI add–drop filters using apodized sub-wavelength grating contradirectional couplers," *Opt. Lett.*, vol. 44, pp. 4929–4932, 2019.
[125] F. O. Afzal, Y. Bian, B. Peng, et al., "O-band subwavelength grating filters in a monolithic photonics technology," *IEEE Photonics Technol. Lett.*, vol. 32, pp. 1207–1210, 2020.
[126] K. Wang, Y. Wang, X. Guo, Y. Zhang, A. He, and Y. Su, "Ultracompact bandwidth-tunable filter based on subwavelength grating-assisted contra-directional couplers," *Front. Optoelectron.*, 2020. https://doi.org/10.1007/s12200-020-1056-5.
[127] N. Wu and L. Xia, "Side-mode suppressed filter based on anangular grating-subwavelength grating microring resonator with high flexibility in wavelength design," *Appl. Opt.*, vol. 58, pp. 7174–7180, 2019.
[128] J. Chen, "A broadband wavelength demultiplexer assisted by SWG-based directional couplers," *Optik (Stuttg)*, vol. 202, p. 163602, 2020.
[129] Y. He, Y. Zhang, Q. Zhu, et al., "Silicon high-order mode (De) multiplexer on single polarization," *J. Light. Technol.*, vol. 36, pp. 5746–5753, 2018.
[130] W. Jiang, J. Miao, T. Li, and L. Ma, "Ultrabroadband and fabrication-tolerant mode (de)multiplexer using subwavelength structure," *J. Opt. Soc. Am. B*, vol. 36, pp. 3125–3132, 2019.
[131] W. Jiang, J. Miao, T. Li, and L. Ma, "On-chip silicon dual-mode multiplexer via a subwavelength grating-based directional coupler and a mode blocker," *Appl. Opt.*, vol. 58, pp. 9290–9296, 2019.
[132] Y. He, Y. Zhang, H. Wang, L. Sun, and Y. Su, "Design and experimental demonstration of a silicon multi-dimensional (de) multiplexer for wavelength-, mode- and polarization-division (de)multiplexing," *Opt. Lett.*, vol. 45, pp. 2846–2849, 2020.
[133] L. Xu, M. Jacques, D. V. Plant, et al., "Ultra-broadband and compact two-mode multiplexer based on subwavelength-grating-slot-assisted adiabatic coupler for the silicon-on-insulator platform," *J. Light. Technol.*, vol. 37, pp. 5790–5800, 2019.
[134] D. Guo and T. Chu, "Silicon mode (de)multiplexers with parameters optimized using shortcuts to adiabaticity," *Opt. Express*, vol. 25, pp. 9160–9170, 2017.
[135] D. González-Andrade, J. G. Wangüemert-Pérez, A. Velasco, et al., "Ultra-broadband mode converter and multiplexer based on sub-wavelength structures," *IEEE Photonics J.*, vol. 10, p. 2201010, 2018.
[136] D. González-Andrade, A. Dias, J. G. Wangüemert-Pérez, et al., "Experimental demonstration of a broadband mode converter and multiplexer based on subwavelength grating waveguides," *Opt. Laser Technol.*, vol. 129, p. 106297, 2020.

[137] D. Taillaert, P. Bienstman, and R. Baets, "Compact efficient broadband grating coupler for silicon-on-insulator waveguides," *Opt. Lett.*, vol. 29, pp. 2749–2751, 2004.
[138] M. J. R. Heck, "Highly integrated optical phased arrays: photonic integrated circuits for optical beam shaping and beam steering," *Nanophotonics*, vol. 6, pp. 93–107, 2017.
[139] R. Marchetti, C. Lacava, L. Carroll, K. Gradkowski, and P. Minzioni, "Coupling strategies for silicon photonics integrated chips [Invited]," *Photonics Res*, vol. 7, pp. 201–239, 2019.
[140] P. Cheben, P. J. Bock, J. H. Schmid, et al., "Refractive index engineering with subwavelength gratings for efficient microphotonic couplers and planar waveguide multiplexers," *Opt. Lett.*, vol. 35, pp. 2526–2528, 2010.
[141] V. R. Almeida, R. R. Panepucci, and M. Lipson, "Nanotaper for compact mode conversion," *Opt. Lett.*, vol. 28, pp. 1302–1304, 2003.
[142] J. D. Sarmiento-Merenguel, A. Ortega-Moñux, J.-M. Fédéli, et al., "Controlling leakage losses in subwavelength grating silicon metamaterial waveguides," *Opt. Lett.*, vol. 41, pp. 3443–3446, 2016.
[143] N. Hatori, T. Shimizu, M. Okano, et al., "A hybrid integrated light source on a silicon platform using a trident spot-size converter," *J. Light. Technol.*, vol. 32, pp. 1329–1336, 2014.
[144] M. Teng, B. Niu, K. Han, S. Kim, Y. Xuan, Y. J. Lee, and M. Qi, "Trident shape SOI metamaterial fiber-to-chip edge coupler," in Optical Fiber Communication Conference (OFC), OSA, 2019, p. Tu2J.6. https://doi.org/10.1364/ofc.2019.tu2j.6.
[145] A. He, X. Guo, K. Wang, Y. Zhang, and Y. Su, "Low loss, large bandwidth fiber-chip edge couplers based on silicon-on-insulator platform," *J. Light. Technol.*, vol. 38, pp. 4780–4786, 2020.
[146] Y. Wang, W. Shi, X. Wang, et al., "Design of broadband subwavelength grating couplers with low back reflection," *Opt. Lett.*, vol. 40, pp. 4647–4650, 2015.
[147] E. W. Ong, T. Wallner, N. M. Fahrenkopf, and D. D. Coolbaugh, "High positional freedom SOI subwavelength grating coupler (SWG) for 300 mm foundry fabrication," *Opt. Express*, vol. 26, pp. 28773–28792, 2018.
[148] X. Chen and H. K. Tsang, "Polarization-independent grating couplers for silicon-on-insulator nanophotonic waveguides," *Opt. Lett.*, vol. 36, pp. 796–798, 2011.
[149] W. Zhou, Z. Cheng, X. Sun, and H. K. Tsang, "Tailorable dual-wavelength-band coupling in a transverse-electric-mode focusing subwavelength grating coupler," *Opt. Lett.*, vol. 43, pp. 2985–2988, 2018.
[150] D. Gostimirovic and W. N. Ye, "An open-source artificial neural network model for polarization-insensitive silicon-on-insulator subwavelength grating couplers," *IEEE J. Sel. Top. Quantum Electron.*, vol. 25, pp. 1–5, 2019.
[151] D. Melati, Y. Grinberg, M. Kamandar Dezfouli, et al., "Mapping the global design space of nanophotonic components using machine learning pattern recognition," *Nat. Commun.*, vol. 10, p. 4775, 2019.
[152] S. Li, L. Cai, D. Gao, et al., "Deterministic design of focusing apodized subwavelength grating coupler based on weak form and transformation optics," *Opt. Express*, vol. 28, pp. 35395–35412, 2020.
[153] M. Kamandar Dezfouli, Y. Grinberg, D. Melati, et al., "Perfectly vertical surface grating couplers using subwavelength engineering for increased feature sizes," *Opt. Lett.*, vol. 45, pp. 3701–3704, 2020.
[154] Z. Zhang, X. Chen, Q. Cheng, et al., "High-efficiency apodized bidirectional grating coupler for perfectly vertical coupling," *Opt. Lett.*, vol. 44, pp. 5081–5084, 2019.
[155] Z. Zhang, X. Chen, Q. Cheng, et al., "Two-dimensional apodized grating coupler for optical coupling," *J. Lightwave Technol.*, vol. 38, pp. 4037–4044, 2020.
[156] N. Chen, B. Dong, X. Luo, et al., "Efficient and broadband subwavelength grating coupler for 3.7 μm mid-infrared silicon photonics integration," *Opt. Express*, vol. 26, pp. 26242–26256, 2018.
[157] W. Zhou and H. K. Tsang, "Dual-wavelength-band subwavelength grating coupler operating in the near infrared and extended shortwave infrared," *Opt. Lett.*, vol. 44, pp. 3621–3624, 2019.
[158] Y. Tong, W. Zhou, X. Wu, and H. K. Tsang, "Efficient mode multiplexer for few-mode fibers using integrated silicon-on-insulator waveguide grating coupler," *IEEE J. Quantum Electron.*, vol. 56, pp. 1–7, 2020.
[159] C. V. Poulton, M. J. Byrd, M. Raval, et al., "Large-scale silicon nitride nanophotonic phased arrays at infrared and visible wavelengths," *Opt. Lett.*, vol. 42, pp. 21–24, 2017.
[160] P. Ginel-Moreno, D. Pereira-Martín, A. Hadij-ElHouati, et al., "Highly efficient optical antenna with small beam divergence in silicon waveguides," *Opt. Lett.*, vol. 45, pp. 5668–5671, 2020.
[161] P. Ginel-Moreno, A. Sánchez-Postigo, J. De-Oliva-Rubio, et al., "Millimeter-long metamaterial surface-emitting antenna in silicon photonics platform," *Opt. Lett.*, vol. 46, pp. 3733–3736, 2021.
[162] S. Khajavi, D. Melati, P. Cheben, et al., "Compact and highly-efficient broadband surface grating antenna on a silicon platform," *Opt. Express*, vol. 29, pp. 17–21, 2021.
[163] M. Soler, O. Calvo-Lozano, M.-C. Estevez, and L. M. Lechuga, "Nanophotonic biosensors: driving personalized medicine," *Opt. Photonics News*, vol. 31, pp. 24–31, 2020.
[164] M. C. C. Estevez, M. Alvarez, and L. M. L. M. Lechuga, "Integrated optical devices for lab-on-a-chip biosensing applications," *Laser Photonics Rev.*, vol. 6, pp. 463–487, 2012.
[165] J. Gonzalo Wangüemert-Pérez, P. Cheben, A. Ortega-Moñux, et al., "Evanescent field waveguide sensing with subwavelength grating structures in silicon-on-insulator," *Opt. Lett.*, vol. 39, pp. 4442–4445, 2014.
[166] V. Donzella, A. Sherwali, J. Flueckiger, S. M. Grist, S. T. Fard, and L. Chrostowski, "Design and fabrication of SOI micro-ring resonators based on sub-wavelength grating waveguides," *Opt. Express*, vol. 23, pp. 4791–4803, 2015.
[167] J. Flueckiger, S. Schmidt, V. Donzella, et al., "Sub-wavelength grating for enhanced ring resonator biosensor," *Opt. Express*, vol. 24, pp. 15672–16686, 2016.
[168] J. G. Wangüemert-Pérez, A. Hadij-ElHouati, A. Sánchez-Postigo, et al., "[INVITED] Subwavelength structures for silicon photonics biosensing," *Opt. Laser Technol.*, vol. 109, pp. 437–448, 2019.

[169] J. Milvich, D. Kohler, W. Freude, and C. Koos, "Surface sensing with integrated optical waveguides: a design guideline," *Opt. Express*, vol. 26, pp. 19885–19906, 2018.
[170] J. R. Bickford, P. S. Cho, M. E. Farrell, E. L. Holthoff, and P. M. Pellegrino, "The investigation of subwavelength grating waveguides for photonic integrated circuit based sensor applications," *IEEE J. Sel. Top. Quantum Electron.*, vol. 25, p. 8200410, 2019.
[171] D. M. Kita, J. Michon, S. G. Johnson, and J. Hu, "Are slot and subwavelength grating waveguides better than strip waveguides for sensing?" *Optica*, vol. 5, pp. 1046–1054, 2018.
[172] M. Odeh, K. Twayana, K. Sloyan, J. E. Villegas, S. Chandran, and M. S. Dahlem, "Mode sensitivity analysis of subwavelength grating slot waveguides," *IEEE Photonics J*, vol. 11, p. 2700210, 2019.
[173] E. Luan, H. Yun, L. Laplatine, et al., "Enhanced sensitivity of subwavelength multibox waveguide microring resonator label-free biosensors," *IEEE J. Sel. Top. Quantum Electron.*, vol. 25, pp. 1–11, 2019.
[174] L. Chrostowski, S. Grist, J. Flueckiger, et al, "Silicon photonic resonator sensors and devices," in A. V. Kudryashov, A. H. Paxton, and V. S. Ilchenko, Eds., 2012. p. 823620. https://doi.org/10.1117/12.916860.
[175] C. W. Chang, X. Xu, S. Chakravarty, et al., "Pedestal subwavelength grating metamaterial waveguide ring resonator for ultra-sensitive label-free biosensing," *Biosens. Bioelectron.*, vol. 141, p. 111396, 2019.
[176] E. Luan, K. M. Awan, K. C. Cheung, and L. Chrostowski, "High-performance sub-wavelength grating-based resonator sensors with substrate overetch," *Opt. Lett.*, vol. 44, pp. 5981–5984, 2019.
[177] E. Luan, H. Yun, M. Ma, D. M. Ratner, K. C. Cheung, and L. Chrostowski, "Label-free biosensing with a multi-box sub-wavelength phase-shifted Bragg grating waveguide," *Biomed. Opt. Express*, vol. 10, pp. 4825–4838, 2019.
[178] P. Xu, J. Zheng, J. Zhou, Y. Chen, C. Zou, and A. Majumdar, "Multi-slot photonic crystal cavities for high-sensitivity refractive index sensing," *Opt. Express*, vol. 27, pp. 3609–3616, 2019.
[179] S. Heinsalu, Y. Isogai, Y. Matsushima, H. Ishikawa, and K. Utaka, "Record-high sensitivity compact multi-slot sub-wavelength Bragg grating refractive index sensor on SOI platform," *Opt. Express*, vol. 28, pp. 28126–28139, 2020.
[180] L. Torrijos-Morán, A. Griol, and J. García-Rupérez, "Experimental study of subwavelength grating bimodal waveguides as ultrasensitive interferometric sensors," *Opt. Lett.*, vol. 44, pp. 4702–4705, 2019.
[181] K. E. Zinoviev, A. B. González-Guerrero, C. Dominguez, and L. M. Lechuga, "Integrated bimodal waveguide interferometric biosensor for label-free analysis," *J. Light. Technol.*, vol. 29, pp. 1926–1930, 2011.
[182] D. Yang, B. Duan, X. Liu, A. Wang, X. Li, and Y. Ji, "Photonic crystal nanobeam cavities for nanoscale optical sensing: a review," *Micromachines*, vol. 11, p. 72, 2020.
[183] Í. Molina-Fernández, J. Leuermann, A. Ortega-Moñux, J. G. Wangüemert-Pérez, and R. Halir, "Fundamental limit of detection of photonic biosensors with coherent phase read-out," *Opt. Express*, vol. 27, pp. 12616–12629, 2019.
[184] R. A. Soref, S. J. Emelett, and W. R. Buchwald, "Silicon waveguided components for the long-wave infrared region," *J. Opt. A Pure Appl. Opt.*, vol. 8, pp. 840–848, 2006.
[185] D. Marris-Morini, V. Vakarin, J. M. Ramirez, et al., "Germanium-based integrated photonics from near- to mid-infrared applications," *Nanophotonics*, vol. 7, pp. 1781–1793, 2018.
[186] Y. Zou, S. Chakravarty, C.-J. Chung, X. Xu, and R. T. Chen, "Mid-infrared silicon photonic waveguides and devices [Invited]," *Photonics Res.*, vol. 6, pp. 254–276, 2018.
[187] T. Hu, B. Dong, X. Luo, et al., "Silicon photonic platforms for mid-infrared applications [Invited]," *Photonics Res.*, vol. 5, p. 417, 2017.
[188] T. Baehr-Jones, A. Spott, R. Ilic, et al., "Silicon-on-sapphire integrated waveguides for the mid-infrared," *Opt. Express*, vol. 18, pp. 12127–12135, 2010.
[189] S. Khan, J. Chiles, J. Ma, and S. Fathpour, "Silicon-on-nitride waveguides for mid- and near-infrared integrated photonics," *Appl. Phys. Lett.*, vol. 102, pp. 2013–2016, 2013.
[190] Z. Cheng, X. Chen, C. Y. Wong, K. Xu, and H. K. Tsang, "Mid-infrared suspended membrane waveguide and ring resonator on silicon-on-insulator," *IEEE Photonics J.*, vol. 4, pp. 1510–1519, 2012.
[191] A. Sánchez-Postigo, J. G. Wangüemert-Pérez, J. S. Penadés, et al., "Mid-infrared suspended waveguide platform and building blocks," *IET Optoelectron*, vol. 13, pp. 55–61, 2019.
[192] J. Soler Penadés, C. Alonso-Ramos, A. Z. Khokhar, et al., "Suspended SOI waveguide with sub-wavelength grating cladding for mid-infrared," *Opt. Lett.*, vol. 39, pp. 5661–5664, 2014.
[193] J. Soler-Penades, A. Ortega-Moñux, M. Nedeljkovic, et al., "Suspended silicon mid-infrared waveguide devices with subwavelength grating metamaterial cladding," *Opt. Express*, vol. 24, pp. 22908–22916, 2016.
[194] Y. Wu, Z. Qu, A. Osman, et al., "Mid-infrared nanometallic antenna assisted silicon waveguide based bolometers," *ACS Photonics*, vol. 6, pp. 3253–3260, 2019.
[195] J. Soler-Penadés, A. Sánchez-Postigo, M. Nedeljkovic, et al., "Suspended silicon waveguides for long-wave infrared wavelengths," *Opt. Lett.*, vol. 43, pp. 795–798, 2018.
[196] Z. Zhang, G. I. Ng, T. Hu, et al., "Mid-infrared sensor based on a suspended microracetrack resonator with lateral subwavelength-grating metamaterial cladding," *IEEE Photonics J.*, vol. 10, p. 6801608, 2018.
[197] W. Zhou, Z. Cheng, X. Wu, X. Sun, and H. K. Tsang, "Fully suspended slot waveguide platform," *J. Appl. Phys.*, vol. 123, 2018, Art no. 063103.
[198] A. Sánchez-Postigo, A. Ortega-Moñux, J. Soler Penadés, et al., "Suspended germanium waveguides with subwavelength-grating metamaterial cladding for the mid-infrared band," *Opt. Express*, vol. 29, pp. 16867–16878, 2021.
[199] A. Sánchez-Postigo, A. Ortega-Moñux, D. Pereira-Martín, et al., "Design of a suspended germanium micro-antenna for efficient fiber-chip coupling in the long-wavelength mid-infrared range," *Opt. Express*, vol. 27, pp. 22302–22315, 2019.

[200] F. Garrisi, I. Chatzopoulos, R. Cernansky, and A. Politi, "Silicon carbide photonic platform based on suspended subwavelength waveguides," *J. Opt. Soc. Am. B*, vol. 37, pp. 3453–3460, 2020.
[201] J. Li, and J. B. Pendry, "Hiding under the carpet: a new strategy for cloaking," *Phys. Rev. Lett.*, vol. 101, p. 203901, 2008.
[202] K. Giewont, S. Hu, B. Peng, et al., "300-mm monolithic silicon photonics foundry technology," *IEEE J. Sel. Top. Quantum Electron.*, vol. 25, pp. 1–11, 2019.
[203] D. Fowler, P. Grosse, F. Gays, B. Szelag, C. Baudot, N. Vuillet, J. Planchot, and F. Boeuf, "Fiber grating coupler development for Si-photonics process design kits at CEA-LETI," in *Smart Photonic and Optoelectronic Integrated Circuits XXI*, vol. 1092205, E.-H. Lee, and S. He, Eds, SPIE, 2019, p. 4.
[204] S. Y. Siew, B. Li, F. Gao, et al., "Review of silicon photonics technology and platform development," *J. Light. Technol.*, vol. 39, pp. 4374–4389, 2021.
[205] J. M. Luque-González, A. Ortega-Moñux, R. Halir, et al., "Bricked subwavelength gratings: a tailorable on-chip metamaterial topology," *Laser Photon. Rev.*, vol. 15, p. 2000478, 2021.

Supplementary material: The online version of this article offers supplementary material (https://doi.org/10.1515/nanoph-2021-0110).